International Journal of Multiphase Flow 149 (2022) 103985

Contents lists available at ScienceDirect

International Journal of Multiphase Flow

journal homepage: www.elsevier.com/locate/ijmulflow

Effect of solid particles on the slug frequency, bubble velocity and bubble length of intermittent gas–liquid two-phase flows in horizontal pipelines

Paolo Sassi [a,b,*], Gonzalo Fernández [b], Youssef Stiriba [a], Jordi Pallarès [a]

[a] Departament d'Enginyeria Mecànica, Universitat Rovira i Virgili, Tarragona, Spain
[b] IMFIA, Facultad de Ingeniería, Universidad de la República, Montevideo, Uruguay

ARTICLE INFO

Keywords:
Gas–liquid–solid three-phase flows
Horizontal pipelines
Slug parameters
Gas–liquid two-phase flow
Image processing

ABSTRACT

New experimental data are presented in this study for intermittent two and three-phase flows through horizontal pipelines involving air, water and polypropylene pellets of sizes ranging between 1 and 2 millimeters. Flow visualization and pressure measurements were performed and are explored in this work for intermittent flows. An automated image processing algorithm is developed to determine slug parameters of 59 flow conditions and compared with other measurements techniques. Correlations available in the literature for predicting slug frequency are tested with the new experimental data and curves of non-dimensional parameters are fitted to the data, the best fitting is obtained for the gas based Strouhal number against the input liquid or gas fraction. The influence of solid particles over the slug frequency is analyzed and reported. A decrease on the slug frequency is found when increasing solid concentrations. Finally, the influence of solid particles on the bubble length and velocity is investigated. A stronger influence of the gas flow rate on the velocity of the nose of the slug is observed for increasing solid concentration, together with more variability on the mean velocity. Also, longer bubbles are obtained with higher solid concentrations.

1. Introduction

Gas–liquid two-phase flows have been the focus of numerous studies, mostly related to the oil and chemical industries. However, gas–liquid–solid (GLS) three-phase flows, which can also be found in these production fields, have not been studied as extensively as two-phase flows. In the oil industry, fragments of sand or solids are often present in the pipes. In the chemical industry many products are comprised of solid particles that can eventually be formed from chemical reactions involving gas and liquid phases. For example GLS phases coexist along the flash lines of some polymerization reactors (Martínez et al., 2017). Some authors have already reported the influence of the solid phase on important parameters such as the flow regime (Sassi et al., 2020b) or the frictional pressure gradient (FPG) (Rahman et al., 2013; Rosas et al., 2018; Sassi et al., 2020b). Other authors focused on the sand deposition in pipelines. For example, Ibarra et al. (2017) carried out experimental and theoretical analysis of critical sand-deposition velocities in gas–liquid–sand stratified flows, later modeled in CFD in Dabirian et al. (2017). A four layer model was developed by Dabirian et al. (2018) for estimating the sand bed height in stratified flows. Dabirian et al. (2019) evaluates the models of Danielson (2007) for predicting the sand deposition velocity in intermittent flows. Beyond these studies, most of the available literature on GLS three-phase flows focuses on the transport of solids, without further analysis on the influence of solids on flow dynamics.

A deep understanding and prediction of the fluid dynamics of multi-phase flow systems is crucial for the design and construction of processes in these industries. Numerical studies are often a very useful tool to assist in the design process (Pineda-Pérez et al., 2018; Akhlaghi et al., 2019). However, to obtain reliable results it is necessary to validate the numerical models with experimental data, which represent an essential and very helpful tool to thoroughly understand the dynamics and interaction of the different phases involved. Flow regime, frictional pressure drop, hold-up (or void fraction) and deposition velocity are all essential parameters for multi-phase facility design. These parameters are in general governed by basic characteristics such as flow orientation (Lu et al., 2018), pipeline diameter (Taitel and Dukler, 1976; Kong et al., 2018a), superficial velocities and slippage (Kong et al., 2018c), and the physical properties of fluids and solids (Bhagwat and Ghajar, 2014).

Intermittent two-phase flow regimes, such as plug and slug flows, are characterized by having two clear differentiated structures, which move intermittently along the pipe, both in space and time (see Fig. 1). These are: (i) a liquid pocket filling the cross section of the pipe, which might contain dispersed bubbles in the case of slug flows and very

* Corresponding author at: Departament d'Enginyeria Mecànica, Universitat Rovira i Virgili, Tarragona, Spain.
E-mail address: psassi@fing.edu.uy (P. Sassi).

https://doi.org/10.1016/j.ijmultiphaseflow.2022.103985
Received 25 May 2021; Received in revised form 1 January 2022; Accepted 17 January 2022
Available online 31 January 2022

Nomenclature

Variables

A	Cross-sectional area [m^2]
C_s	Solid concentration (volume fraction)
D	Internal diameter of the pipe [m]
d	Particle diameter [m]
f	Frequency [Hz]
Fr	Froude number, $Fr = U^2/gD$
G	Mass flow rate [g/s]
g	Acceleration of gravity (9.81 m/s^2)
H	Hold-up
j	Superficial velocity [m/s]
L	Length [m]
P	Pressure [Pa]
Re	Reynolds number, $Re = UD/\nu$
St	Strouhal number, $St = fD/U$
T	Temperature [°C]
t	Time [s]
U	Velocity [m/s]
z	Axial coordinate [m]
f	Darcy–Weisbach friction factor

Greek Symbols

α	Void fraction
λ	Input fraction ($\lambda_f = \frac{j_f}{U_M}$)
μ	Dynamic viscosity [Pa s]
ν	Kinematic viscosity [m^2/s]
ρ	Density [kg/m^3]

Subscripts

atm	Atmospheric conditions
b	Bubble
f	Liquid phase indicator
g	Gas phase indicator
lp	Liquid pocket
M	Mixture indicator
mod	Modified
S	Slug
s	Solid phase indicator

Abbreviations

G/L	Gas–liquid mixture
$G/L/S$	Gas–liquid–solid mixture
AAPD	Averaged absolute percentage difference
APD	Averaged percentage difference
DAS	Data acquisition system
FPG	Frictional pressure gradient
FPS	Frames per second
LESLIE	Low prESsure muLtIphasE flow loop
LSI	Line-scan image
MSE	Mean squared error
PT	Pressure tap
RMSPD	Root mean squared percentage difference
VDF	Variable frequency drive

few or even none bubbles in plug flows, followed by (ii) an elongated bubble at the top of the pipe traveling over a film of liquid that lays at the bottom. Both structures, considered together, conform the slug unit cell. Fig. 1 shows schematic slug units both for plug (left) and slug (right) flows. The main differences between plug and slug flow regimes are that in plug flows, elongated bubbles exhibit round and smooth noses without any significant detachment of small bubbles into the liquid pockets. Whereas in slug flows the interface of the elongated bubbles is wavy, the nose present a bullet shape and several small bubbles are detached from the elongated bubbles into the liquid pockets (entrained gas fraction). The transition between plug and slug regimes has been addressed in a previous publication (Sassi et al., 2020b) for two and three phase flows, however there is not a general consensus on how to differentiate these two regimes (Arabi et al., 2020a, 2021). More details on plug and slug flows characteristics and the transition between these regimes can be found in Talley et al. (2015), Kong et al. (2018b), Thaker and Banerjee (2017) and Sassi et al. (2020a). Moreover, the influence of solid particles in the dynamics of intermittent flows are reported in Sassi et al. (2020b) and Rosas et al. (2018).

Comprehensive understanding of multi-phase flows is important for several aspects of the industry, specially when intermittent flows are involved. On the one hand, several industries try to avoid the operation in these flow regimes, such is the case of the oil industry, where control strategies are developed to mitigate or reduce intermittent flows (Godhavn et al., 2005). The constant presence of intermittent flows can be destructive for the pipelines in the long term, due to the impact that it exerts on the momentum and frictional pressure gradient, especially for long piping systems, where flow rates can fluctuate significantly both in space and time and may induce vibrations (Deendarlianto et al., 2019). Moreover, the slug frequency (the number of slug unit cells that pass through a specific cross section in the pipe per time unit), which can also vary for different settings, could eventually lead to resonance problems (Thaker and Banerjee, 2016b). Furthermore, it can also drive to flow induced corrosion (Thaker and Banerjee, 2016a) and flow accelerated corrosion (Zhai et al., 2018).

On the other hand, numerous processes, mainly in the chemical industry, require the presence of intermittent flows for ensuring the efficient development of processes, where mass and heat transfer occur through the interface of the phases. In these cases, special criteria must be considered for the construction of the facilities.

The study of the dynamics of intermittent flows entails great complexities, due to the inherent random nature of slug frequency (Al-Safran, 2016). Several phenomena contribute to that randomness, such as slug initiation, break-up and coalescence of elongated bubbles, which are also random processes themselves. Further details on slug initiation and development can be found in Al-Safran (2009).

The prediction of slug frequency has been already addressed by several authors, and different measurement techniques have been developed. Counting slug units from video recordings is a widely used method, especially as a comparison tool due to its high fidelity. Also, the inference of the slug frequency from time signals has been the focus of several studies. Void fraction signals obtained from capacitance or impedance sensors, interface density functions obtained with probes (capacitance or optical) and differential pressure signals are some examples of the signals used in the literature. Furthermore, the most employed approaches to obtain the frequency from the signals are (i) counting peaks above certain threshold and (ii) calculating the power spectral density of the signal to obtain the dominant frequency. Within the counting methods, the Wilkens and Thomas method is based on counting the peaks that reach a certain threshold, on a signal obtained from a differential pressure measurement between two pressure taps. The authors considered that the transit of a liquid pocket between the two taps would produce a greater pressure loss than the presence of an elongated bubble. Table 1 summarizes some relevant studies on slug

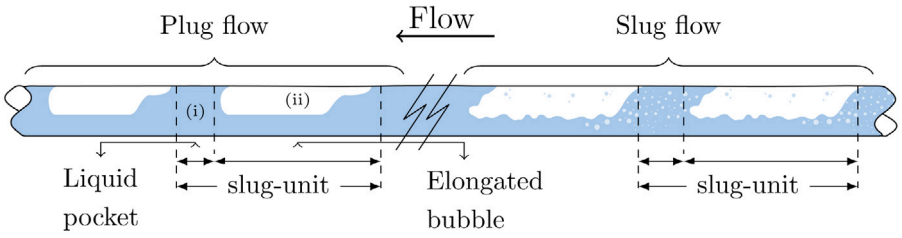

Fig. 1. Scheme of plug and slug flow regimes.

frequency in horizontal pipelines, their corresponding experimental techniques and conditions during the measurements, as well as their main findings or proposed correlations.

Arabi et al. (2020b) and Lin et al. (2013) carried out experimental analyses of the slug frequency using differential pressure signals. Comparison of counting peaks, Wilkens & Thomas and PSD methods were performed. Arabi et al. (2020b) found the best predictions with the PSD, while Lin et al. (2013) obtained the best predictions with the counting method with a lower threshold (Wilkens & Thomas method). Both counting and spectral methods provide precise results for relatively low velocities. However, when flow velocities increase, the slug frequency is no longer dominated by a single frequency, and several frequencies with similar power can be observed. Bertola and Cafaro (2002) also made a comparison between the counting and PSD methods from density function signals obtained with an optical probe. They conclude that despite the better precision obtained with the counting method (±1%) the PSD provides better insight of intermittent flows, as it takes into account the presence of harmonic components. Most of the correlations used for predicting the slug frequency are deterministic, as they provide one single value of frequency. Al-Safran (2016) proposed a probabilistic model, using Poisson probability theory to take into account the random behavior of the slug frequency and also the systematic errors derived from the use of experimental instruments.

For measuring elongated bubbles parameters, such as length and translational velocity several authors proposed different techniques. Thaker and Banerjee (2016b) performed a flow visualization analysis of the slug frequency measuring the time interval between slugs from images taken at 1600 FPS. They also measured bubble length and velocity with image processing. Wang et al. (2007) measured slug frequency, translation velocities of elongated bubbles and lengths of liquid slugs and elongated bubbles with pairs of conductivity probes. They concluded that slug frequency is dependent on Froude number and the distance from the entrance in the higher mixture velocity range. Hout et al. (2002) measured elongated bubbles translational velocity for horizontal and inclined pipes for comparison with available correlations. They cross-correlated the output signals of consecutive optical fiber probes and also used image processing technique. Al-Kayiem et al. (2017) performed optical measurements with high speed camera for characterizing slug frequency, length and translational velocity. They found that the slug parameters depends on the distance from the entrance.

The present study analyzes the slug frequency, velocity and length of intermittent two and three-phase flows, gas–liquid and gas–liquid–solid, respectively. Section 2 describes the experimental setup and the methodology followed with data acquisition and processing, together with sensitivity analysis and calibration of the measurements techniques. The results are discussed in Section 3. First a comparison between different measuring techniques of slug frequency is presented. Then, frequency results for two and three-phase flows are described and the effect of solid particles over the slug frequency is discussed. Correlations for two-phase flow slug frequency are tested and finally measurements of bubble velocity and length are shown. The conclusions of this research work are outlined in Section 4.

2. Experimental facility & methodology

Measurements were performed at the Low prESsure muLtIphasE test loop (LESLIE) installed at the multi-phase flow laboratory of the Universitat Rovira i Virgili (Tarragona, Spain). The facility has 30 mm ID acrylic pipes and was designed for investigating gas–liquid (G/L) and gas–liquid–solid (G/L/S) flows in horizontal and vertical orientations. In the present study, experiments were performed for two and three-phase intermittent flows in the horizontal test section, sketched in Fig. 2. The test cases involved compressed air, water and polypropylene pellets ($d = 1 - 2$ mm, $\rho_s = 866$ kg/m^3) as the gas, liquid and solid phases, respectively. More details of the experimental facility can be found in Sassi et al. (2020a,b).

2.1. Air system

Compressed air is taken from the University line at 8 bar, already filtered and dried. Air flow rates are measured and controlled with an Omega mass flow controller, which uses the principle of differential pressure within a laminar flow field to determine and control mass flow rate with an accuracy of ±0.8% of the reading. Finally, a one-way check valve that is located just before the air is delivered to the mixing chamber. Four air mass flow rates were used during the experiments, 0.75, 1.25, 2.0 and 4.0 g/s.

2.2. Water/slurry system

Tap water is stored in a 100 liter PVC parallelepiped tank. Polypropylene poly-dispersed pellets ranging between 1 and 2 mm were collected with corresponding sieves. For the three-phase flow runs, the solid pellets are added in the tank. An Ebara 7.5 kW centrifugal pump with a 224 mm (AISI316L) closed impeller is used to deliver solid–liquid phases to the test section. A recirculating line from the discharge to the storage tank ensures the mixing of the liquid and solid phases in the tank. The flow rate is measured with an Isoil MS2500 electromagnetic flow meter with an accuracy of ±0.8%. Measurements were carried out for 5 flow rates of liquid (or slurry) which represent superficial velocities in the test section of 0.85, 1.00, 1.5, 2.0 and 2.5 m/s, and for volumetric concentrations of 0% (two-phase), 10% and 20% of polypropylene pellets. The volumetric concentration is calculated with Eq. (1) where V is the volume reading of a graded recipient and C_{max} is the maximum packing concentration, it was determined to be $C_{max} = 0.585$ by submerging the particles in ethanol ($\rho_{ethanol} = 789$ kg/m^3).

$$C_{vol} = \frac{V_{particles} \times C_{max}}{V_{water} + V_{particles} \times C_{max}} \tag{1}$$

2.3. Measurements

Measurements are reported for two and three-phase flows in the plug to slug transition zone with relatively high liquid superficial velocities (or slurry in the case of three-phase flows). The summary of the runs can be seen and compared with the regime map in Fig. 3, the transition from plug to slug flow is indicated with a dashed line for two phase flows and with a dot-dashed line for three-phase flows with 10%

Table 1
Previous studies on slug frequency in horizontal pipelines.

Author	D [mm]	L/D	Superficial velocities [m/s]	Measurement technique	Correlation/findings
Gregory and Scott (1969)	19.1	300	$j_f = 0.6–2$ $j_g = 0.3–8$	Counting liquid slugs from visual observation with stopwatch and counting slug pressure pulses on the strip chart	$f_S = 0.0226\left[\frac{j_f}{gD}\left(\frac{19.75}{U_M}+U_M\right)\right]^{1.2}$
Fetter (1988)	70 82	–	$j_f = 0.1–4$ $j_g = 0.5–20$	Signal processing from clamp-on acoustic two-phase flow-meter. Developed with two accelerometers clamped to the pipe wall (2 meters apart).	$f_S = 0.0175\left[\frac{j_f}{gD}\left(\frac{21.3+U_M^2}{U_M}\right)\right]^{1.37}$
Manolis et al. (1995)	78	363	$j_f = 0.5–1.25$ $j_g = 1–7$	Water hold-up from gamma densitometer at sampling frequency of 25 Hz, two conductivity probes (60 cm. separation) and high spreed video camera (50 FPS).	$f_S = 0.037 Fr_{mod}^{1.8}$, $Fr_{mod} = \frac{j_f}{gD}\left(\frac{U_{M,min}^2+U_M^2}{U_M}\right)$
Bertola and Cafaro (2002)	80	96, 101, 104	$j_f = 0.6–2$ $j_g = 0.3–8$	Counting peaks above threshold and PSD of phase density function from optical probe at 2 kHz.	–
Fossa et al. (2003)	40 60	95, 148, 151, 255 33, 100, 160	$j_f = 0.6–3.0$ $j_g = 0.3–4.0$	Void probability density function from impedance meter (20 kHz) and comparison with slug residence time from fast camera.	$St_g = \frac{f_S D}{j_g} = \frac{0.044\lambda_f}{1-1.71\lambda_f+0.7\lambda_f^2}$
Wang et al. (2007)	50	1157, 2609	$j_f = 0.16–1.5$ $j_g = 1–20$	Reciprocal of slug unit period, calculated with gas–liquid interface density function, from pairs of conductivity probes.	$St_g = \frac{0.05\lambda_f}{1-1.675\lambda_f+0.768\lambda_f^2}$
Wilkens and Thomas (2008)	52	145–280	$j_f = 0.36–0.59$ $j_g = 1.5–10$	Counting peaks above threshold from differential pressure transducers signal.	Wilkens and Thomas method
Al-Safran (2009)[a]	50.8[b]	3898, 6920	$j_f = 0.06–1.2$ $j_g = 0.64–4.27$	Liquid hold-up from capacitance sensors.	$\ln(f_S) =$ $0.8+1.53\ln(U_f)+0.27\left(\frac{U_{slip}}{U_M}\right)-34.1D$ $U_L = \frac{j_f}{H_f}$, $U_{slip} = \frac{j_g}{(1-H_f)}-\frac{j_f}{H_f}$
Thaker and Banerjee (2015)	25	30, 60, 120, 190, 260	$j_f = 0.11–0.74$ $G_g = 0.13–2.6$ g/s	Time interval between slugs calculated from images taken at 1200 FPS.	$f'_S =$ $1.52\times10^{-8}\left(\frac{L}{D}\right)^{-0.14}(Re_f)^{1.45}(Re_g)^{0.28}$
Thaker and Banerjee (2016a)	25	–	$j_f = 0.02–1.14$ $j_g = 0.484–4.312$	Time interval between slugs calculated from fast camera images.	Erosion-corrosion map
Thaker and Banerjee (2016b)	–	–	$j_f = 0.194–0.971$ $j_g = 0.484–3.388$	Time interval between slugs calculated from images taken at 1600 FPS.	$St_M = \frac{0.036\lambda_f}{1-1.432\lambda_f+0.739\lambda_f^2}$
Al-Safran (2016)	25–203	–	$j_f = 0.03–2.89$ $j_g = 0.06–16.5$	Data taken from experimental data base.	$\ln(f_S) =$ $1.51-17.04D+0.77\ln(j_f)-0.181\ln(S)$ $S = \frac{U_g}{U_f} = 1+1.95\left(\frac{\mu_f}{\mu_0}\right)^{0.01}\left(\frac{j_g}{j_f}\right)^{1.5}$
Archibong-Eso et al. (2018)[c]	25.4 76.4	190 220	$j_f = 0.03–0.31$ $j_g = 0.1–7.0$	Counting peaks above threshold of void fraction signals from electrical capacitance. Comparison with counts from visual observation with fast-camera and two gamma densitometers.	$\ln(f_S) = \beta\ln\left[\frac{\lambda}{\varphi^n}\right]$ $\varphi = \left[\frac{D^{3/2}\sqrt{\rho_f(\rho_f-\rho_g)g}}{\mu_f}\right]$ $(\beta,n) = \begin{cases}(0.75, 0.55) & \mathrm{Re}_{SG}\le 2500\\(0.35, 1.02) & \mathrm{Re}_{SG}>2500\end{cases}$
Al-Alweet et al. (2020)	20[b]	170	$j_f = 0–1.06$ $j_g = 0–5$	Frequency and statistical analysis of liquid hold-up signals from two-electrodes capacitance sensor.	Identification of flow patterns
Arabi et al. (2020b)	30	173.3–193.3	$j_f = 0.15–0.8$ $j_g = 0.4–3.6$	Comparison of counting slugs, Wilkens and Thomas and PSD methods using differential pressure transducers signals.	$St_g = \frac{A\lambda_f}{1+B\lambda_f+C\lambda_f^2}$ $A = 0.06327; 0.04071; 0.04234$[d] $B = -1.855; -3.105; -4.271$[d] $C = 1.163; 4.188; 13.860$[d]
Arabi et al. (2020a)	25–76.3	–	$j_f = 0.03–2$ $j_g = 0.046–0.786$	Data taken from experimental data base.	$St_g = \frac{0.03693\lambda_f}{1-1.865\lambda_f+0.9118\lambda_f^2}$

[a] Air/oil as working fluids.
[b] Measurements with inclined orientations are also reported.
[c] Air/water and air/oil as working fluids.
[d] Plug, low aerated slug and highly aerated slug flows.

of solid volumetric concentration. The latter was determined in Sassi et al. (2020b), no line is available for 20% of solid concentration. A total of 20 runs of two-phase flows are indicated with circles while three phase flows with 10% and 20% of volumetric solid concentration are shown with black and red crosses markers respectively. The values of the solid concentration were chosen as representative because in a previous work it was found little impact for 5% of solid concentration. Note that equivalent sets have been used for two and three-phase flows with 10% of solid loading and only 19 runs are reported with 20% of solid concentration (red crosses) as the most demanding setting was

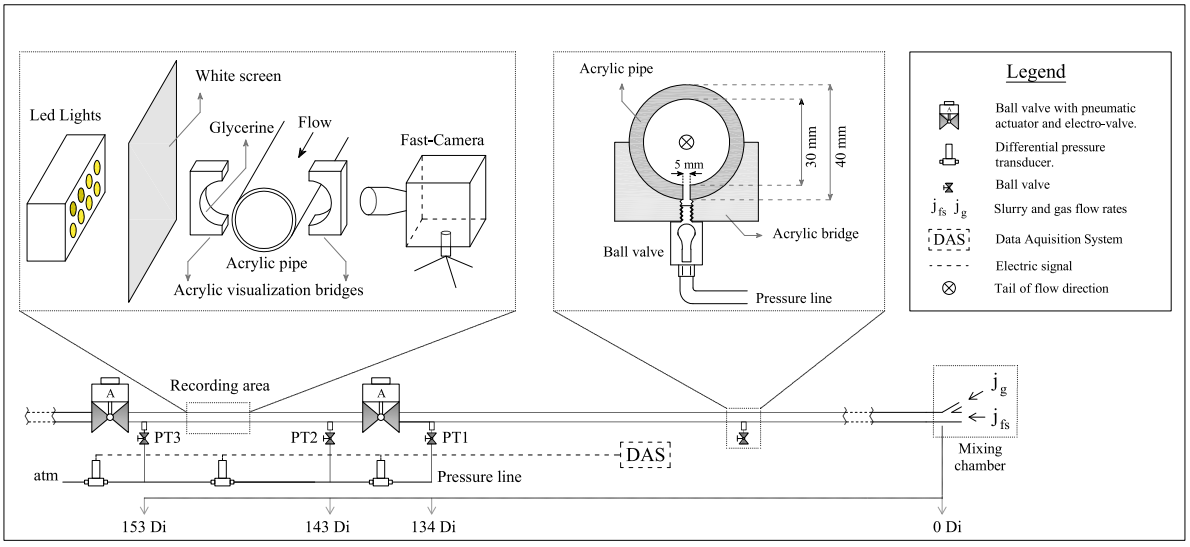

Fig. 2. Schematic of the test section.

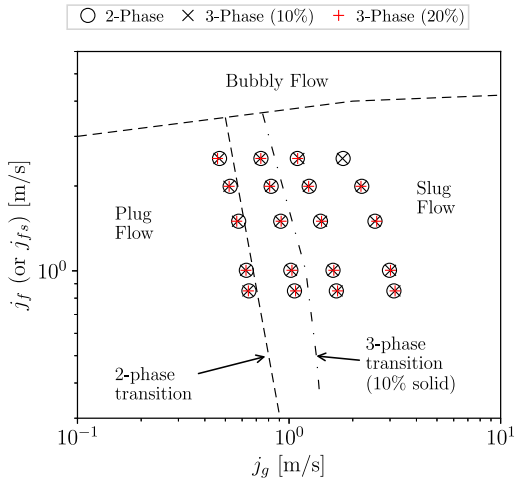

Fig. 3. Summary of experimental runs in the regime map. (For interpretation of the references to color in this figure legend, the reader is referred to the web version of this article.)

beyond the power of the slurry pump. Each flow regime is carefully identified using fast camera recordings and all of them are consistent with the flow regime map limits. More details on the flow regime identification and the transition boundaries are described in Sassi et al. (2020b).

The gas superficial velocity is calculated locally, at the test section, with Eq. (2), where G_g is the mass flow rate reading, A is the cross section area and ρ_g is the gas density. The latter is calculated using the ideal gas equation (Eq. (3)) with the measured absolute local pressure P and the absolute mixture temperature T. Pressure measurements are performed with Omega differential pressure transducers. The differential pressure inside the pipe is measured with a 5 psi transducer and the gauge pressure measurement is preformed with a 15 psi transducer, as indicated in Fig. 2. Data is collected with a data acquisition system (Agilent 34970 A) at 50 samples per second.

$$j_g = \frac{G_g}{\rho_g \cdot A} \tag{2}$$

$$\rho_g = \frac{P}{R_{air} \cdot T} \tag{3}$$

Table 2
Summary of methods for measuring slug frequency.

Method	Approach	Measurement	Output
Line-scan image (LSI)	Counting slug units & residence time in LSI	Fast camera visualization	Distribution of frequencies
Wilkens and Thomas	Counting peaks	Differential pressure	Main frequency
Power spectral density	Fourier analysis	Differential pressure	Power distribution of frequency components
Power spectral density	Fourier analysis	Mean intensity of LSI	Power distribution of frequency components

2.3.1. Slug frequency

Slug frequency is measured with four different methods including counting the peaks above a certain threshold of the static pressure signal and through the power spectral density of the pressure signal. The description of the methods together with examples of the signals can be found in Appendices A and B. A summary of the methods are listed in Table 2.

The slug frequency obtained with the line-scan image (LSI) method is used as the reference method. The LSI is constructed with images taken at 3200 frames per second (FPS) with a Photron Mini UX100 fast camera with a 22 mm lens. Images were captured in the test section, 150 D downstream the mixing chamber when the flow was statistically fully developed, at 3200 frames per second with a resolution of 1×640 pixels in the axial and vertical directions respectively. For each run, 75 s of images were taken, corresponding to a total of 240,000 frames per run. Each image has been pre-processed with background subtraction and histogram stretching to enhance contrast. The line-scan image is made by placing one frame next-to each other. In this way, a $240{,}000 \times 640$ pixels image is obtained. The vertical coordinate of the resulting image corresponds to the vertical axis of the pipe, and the horizontal axis is the evolution in time of the flow state as it passes through the selected cross section (during 75 s).

In the line-scan image, the noses and tails of the elongated bubbles can be easily identified. The upper panel of Fig. 4 shows a portion of the line-scan image corresponding to the first second of a two-phase flow run. The blue and red vertical lines correspond to the location of the noses and tails of the elongated bubbles respectively. In order to identify the noses and tails, the mean intensity of the image is calculated in the vertical axis, zero-meaned and filtered with a low pass filter (moving mean of the signal with a width of 20 samples).

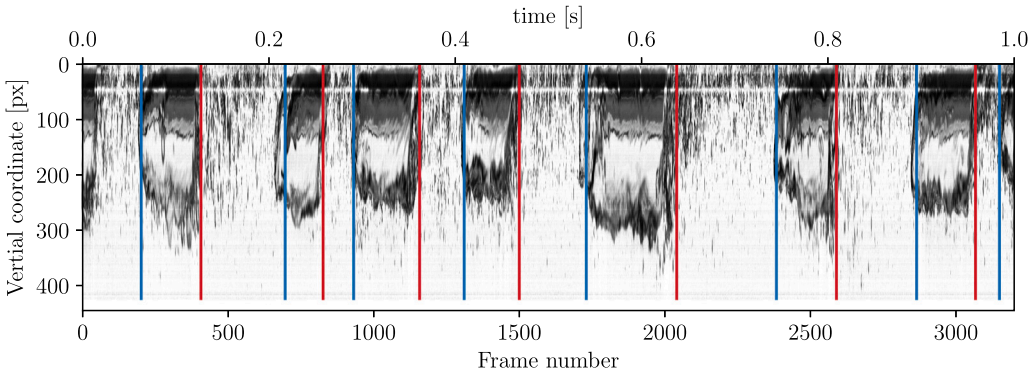

(a) Line-scan image with location of noses (blue) and tails (red lines) of Taylor bubbles.

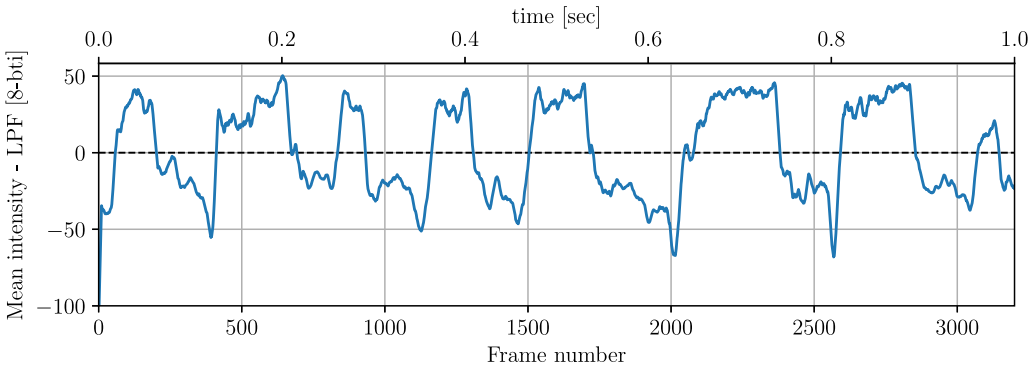

(b) Zero-mean intensity in vertical coordinate with low pass filter.

Fig. 4. Bubbles location for a two-phase flow run, $j_f = 1.5$ m/s and $j_g = 0.58$ m/s. (For interpretation of the references to color in this figure legend, the reader is referred to the web version of this article.)

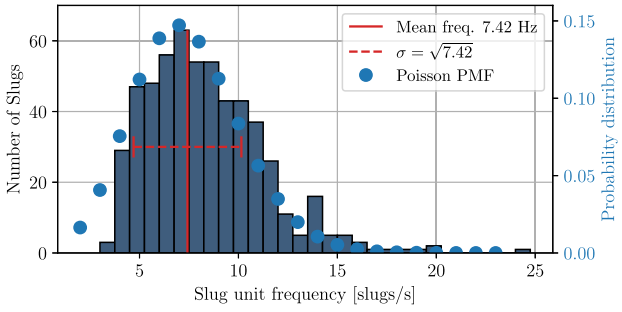

Fig. 5. Slug unit frequency histogram and probability distribution, two-phase flow $j_f = 1.5$ m/s and $j_g = 0.58$ m/s.

The filtered signal corresponding to the line-scan image is plotted in the bottom panel of Fig. 4 for the same time interval. It can be seen that for this particular regime, the filtered signal in the presence of a bubble is less than zero and greater in the presence of a liquid slug. Thus, noses can be identified when the filtered signal crosses the zero downwards and tails when crosses it upwards.

Since the horizontal axis of the line-scan image is a measure of time, the distance between two consecutive noses (two blue lines in Fig. 4) is a measure of the residence time of a slug unit. This is nothing more than the period of an individual slug unit, and therefore its inverse is the frequency. It is then possible to calculate a frequency for each individual slug unit and plot a frequency histogram for each run. Fig. 5 shows the histogram of slug unit frequencies for a two-phase flow with $j_f = 1.5$ m/s and $j_g = 0.58$ m/s. In total, 555 slug units were identified in 75 s, representing an average frequency of 7.4 Hz (red line in Fig. 5).

It can be seen that the histogram from Fig. 5 is right skewed, here the blue dots correspond to the Poisson probability distribution. The distribution fits well the experimental data in the histogram, in agreement with Al-Safran (2016). The red dashed line represents the standard deviation of the distribution, which in the case of the Poisson distribution corresponds to the square root of the mean value.

2.3.2. Bubble velocity & length

Velocity and length of elongated bubbles are also measured with optical techniques. The full methodologies for the bubble length and velocity are described in Appendix B.2 together with its validation, a sensitivity analysis of the method and the pixel size measurement procedure.

3. Results and discussion

Results are presented for two and three-phase flows, including volume concentrations of 10% and 20% of solid. First, the results regarding slug frequency are presented for all runs including mean frequency and frequency distributions. Then, the effect of several parameters on the velocity of the slugs is reported. Finally, the bubble length measurements are discussed.

3.1. Slug frequency

Comparison of different measuring techniques

At the first instance, the four methods for calculating the slug frequency, indicated in Table 2 are compared for two-phase flow, using the frequency obtained with line-scan image method (LSI frequency) as the reference frequency. In Fig. 6 the LSI frequency is in the horizontal axis and the prediction of the rest of the methods in the vertical axis.

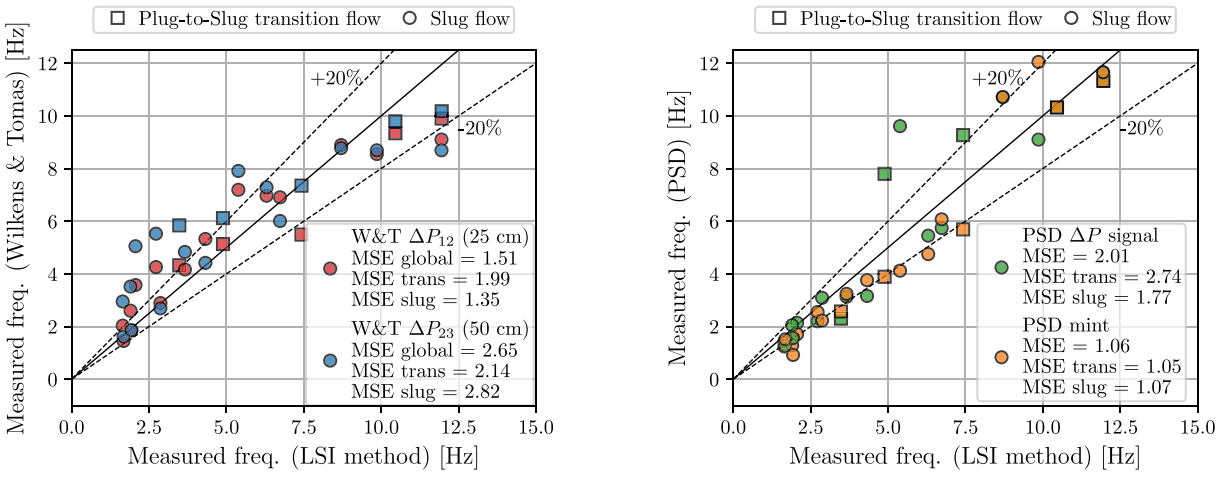

(a) Wilkens & Thomas vs LSI method.

(b) PSD vs LSI method.

Fig. 6. Comparison of different measuring techniques, two-phase flow. (For interpretation of the references to color in this figure legend, the reader is referred to the web version of this article.)

The red and blue symbols correspond to the Wilkens and Thomas method, using 25 and 50 cm of pressure tap spacing (WT_{25} and WT_{50}), respectively. The green symbols represent the frequencies obtained by the power spectral density of the pressure signal. The orange markers are obtained by calculating the dominant frequency of the PSD applied to mean intensity of the line-scan image (Fig. 4b). Squares and circles represent plug-to-slug transition and slug flows, respectively. The mean squared error (MSE), calculated with Eq. (4), is presented for the four methods in the legend.

$$MSE = \frac{1}{n}\sum^{n}\left(f_S - f_S\right)^2 \tag{4}$$

It can be seen that the Wilkens & Thomas method provides some good approximations for the mean frequency, however there are some measurements that exhibit relevant discrepancies. The mean squared error (MSE) for WT_{25} and WT_{50} are 1.5 and 2.65 Hz^2, respectively. For low liquid velocities (and therefore low frequencies) with reduced system pressures, the Wilkens & Thomas method tends to overestimate the slug frequency and as the liquid velocities increase, so does the system pressure, and the measurements become more accurate when compared with the LSI method.

The PSD of the pressure signals provides some good approximations of the main frequency, such is the case of the example from Fig. A.22, where a prominent peak is seen in the three pressure signals. But again, for some runs the deviation from the counting method is significant and the MSE is about 2 Hz^2. Also, in some runs there is not a clear prominent peak in the spectrum, as illustrated in Fig. A.23, where the three PSD's correspond to the same run. In these cases it is hard to obtain a main frequency from the PSD. So, for runs like this, further analysis is required to determine the mean slug frequency.

Finally, by applying the PSD to the LSI signal (see Fig. 4b) better results are obtained with a MSE of 1.06 Hz^2. As an example, the PSD of the signal from Fig. 4b is presented in Fig. B.24. It can be noted that several frequencies have similar energy in a range from about 4 Hz up to 10 Hz. However, the highest peak (at f = 5.69 Hz.), does not correspond to the mean frequency obtained by counting the slug units in the line-scan image (f = 7.42 Hz).

Influence of the concentration of solid phase

The measured slug frequencies for all the runs are presented in Fig. 7, where the LSI frequency is plotted against the liquid (or slurry) superficial velocity. Figs. 7a to 7c correspond to the measurements for two-phase flow and three-phase flow with 10% and 20% of solid loading, respectively. The filled symbols indicate different gas mass flow rates (note that as the liquid velocity increases so does the pressure of the system, and thus the gas velocity decreases for identical mass flow rate). The white, green, yellow and gray markers indicate a gas mass flow rates of 0.75, 1.25, 2.00 and 4.00 g/s, respectively. The dashed lines connect the circles with the same gas mass flow.

Fig. 7 shows the strong influence of the liquid superficial velocity on the slug frequency of two and three-phase flows, which has been already identified and addressed by several authors for gas–liquid two-phase flows systems (Arabi et al., 2020a). It is worth noting that the solids used in these measurements are polypropylene particles, which float in water and tend to accumulate in the upper part of the tube and mainly in the tail of the elongated bubbles (Sassi et al., 2020b). Figs. 7a to 7c reveal that the influence of the gas superficial velocity becomes stronger at higher liquid superficial velocities. This is clearly because of the divergence of the dashed lines as the superficial liquid velocity is increased. Finally, there is a modest influence of the solid phase on the slug frequency. When comparing Figs. 7a to 7b, a slight decrease in the mean frequency is observed in the runs with solid particles. Also when comparing the corresponding runs in Figs. 7b and 7c, another small decrease is shown. These results suggest that, for increasing solid concentrations, there is a decrease of the slug frequency. This could be explained because of the accumulation of solid particles in the tail of the elongated bubbles, that difficults the detachment of the bubbles from the tail, as reported in Sassi et al. (2020b). If the detachment of bubbles is reduced, the elongated bubbles contain more air and therefore appear longer. Longer bubbles for the same set of superficial velocities results in a lower frequency, as fewer slug units will be counted in the same time interval.

Note that the plotted frequencies in Fig. 7 represent the mean frequencies but the slugs are different in size and travel in a certain speed range. So, the slug frequency is not constant and follows a probabilistic distribution, which is well represented by a Poisson distribution (Fig. 5). In Fig. 8 the histograms of the inverse of the permanence time (frequency) of the slug units are illustrated for four operational conditions of two and three-phase runs with 10% and 20% of solid concentration.

The vertical axis in the histograms of Fig. 8 are not normalized and they indicate the number of slug units in the corresponding bin. The red vertical lines indicate the mean frequency, whose values are plotted in Fig. 7. It can be seen that the regimes with lower mean frequencies have a very narrow frequency distribution, whereas the distributions with high mean frequencies are extended over a wide range of frequencies. The complete set of histograms for all the 59 runs are presented in Appendix C.

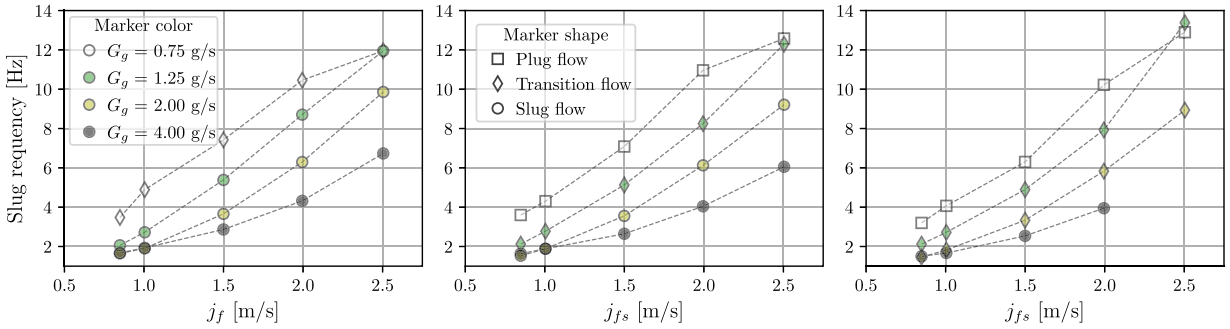

(a) Two-phase flow. (b) Three-phase flow 10% loading (c) Three-phase flow 20% loading

Fig. 7. Slug frequency against liquid superficial velocity for different gas mass flow rates. (For interpretation of the references to color in this figure legend, the reader is referred to the web version of this article.)

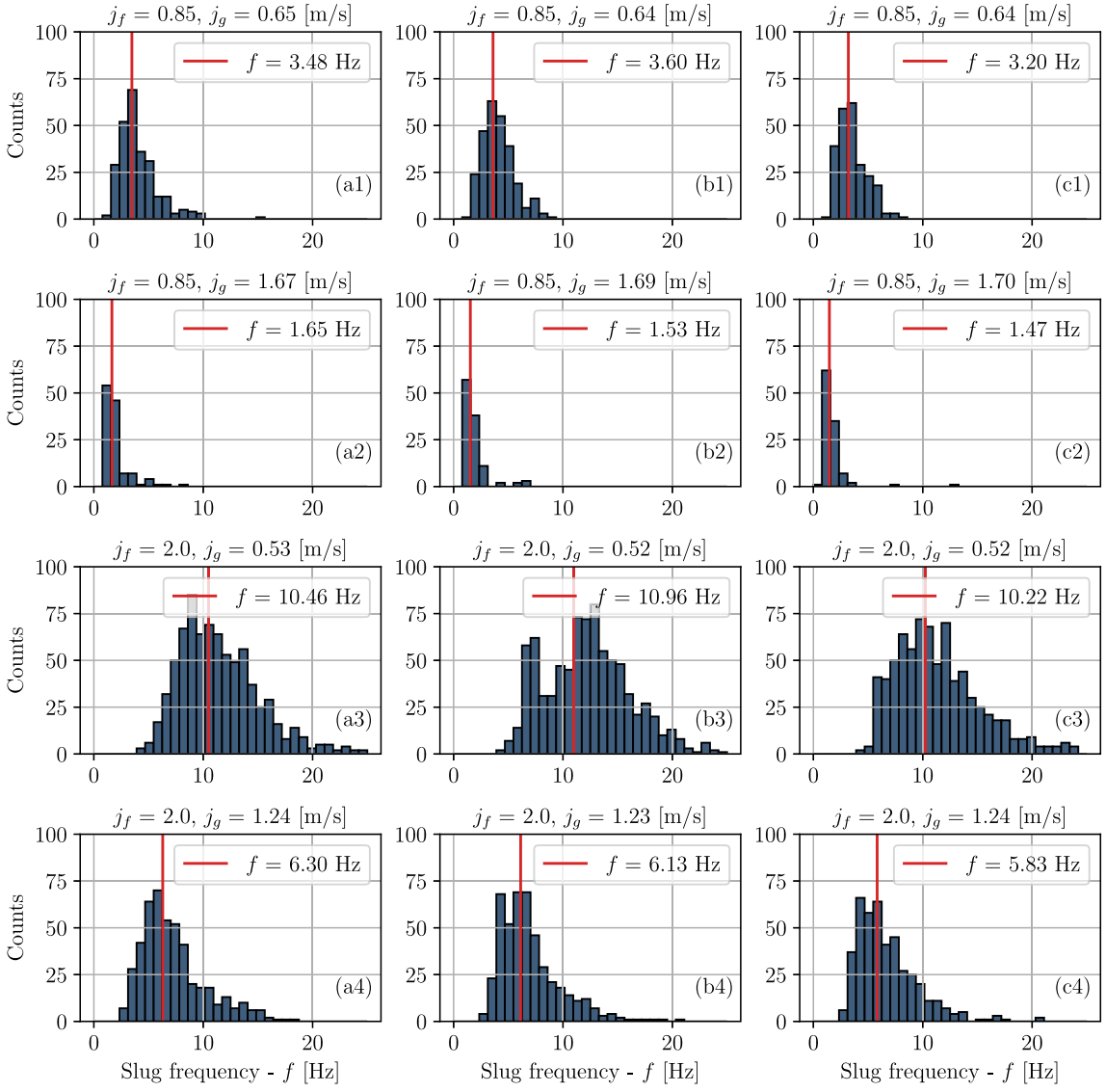

(a) Two-phase flow. (b) Three-phase flow 10% concentration (c) Three-phase flow 20% concentration

Fig. 8. Histograms of measured slug frequencies for three-phase flows with 20% of solid concentration.

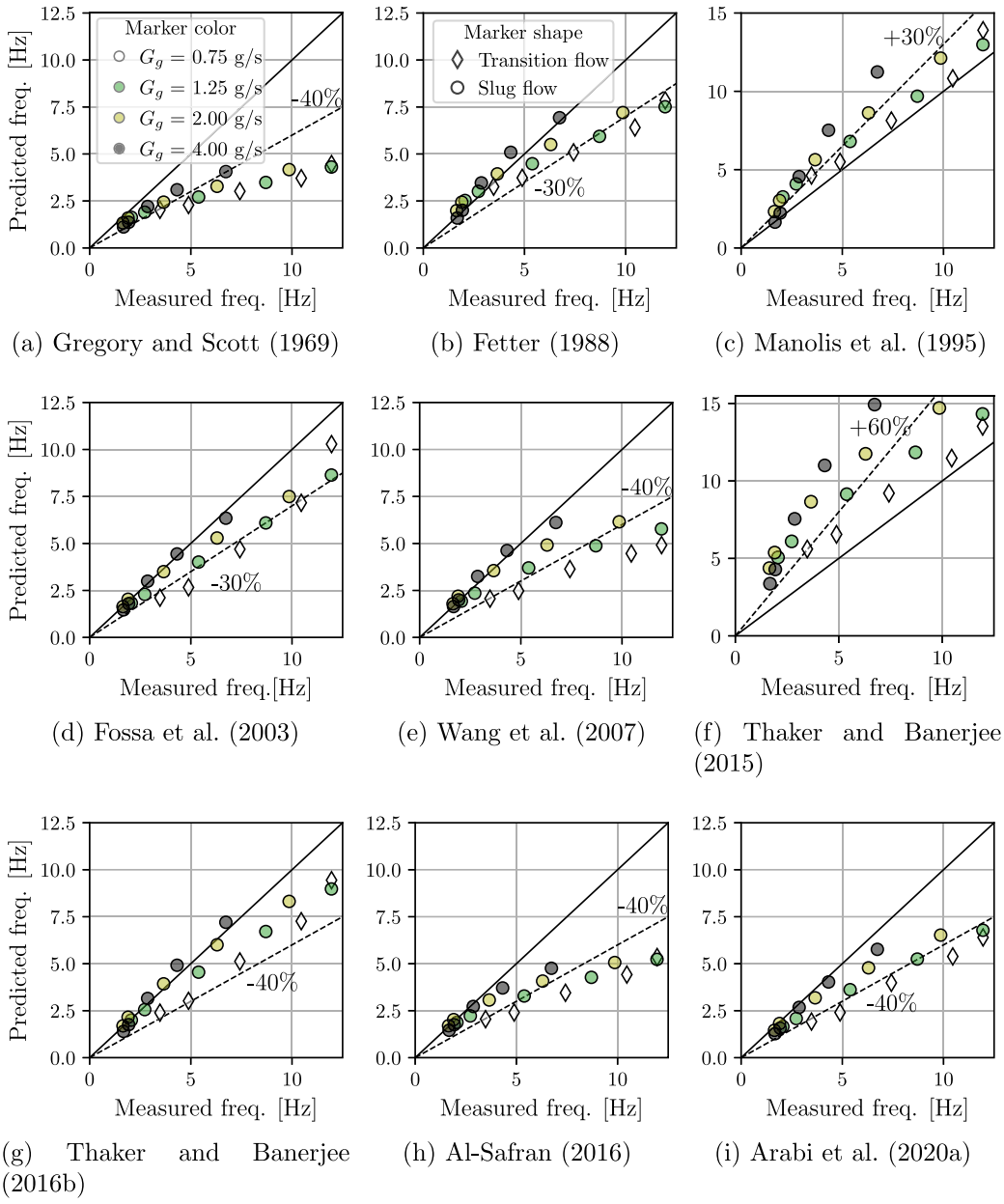

Fig. 9. Comparison of correlations. (For interpretation of the references to color in this figure legend, the reader is referred to the web version of this article.)

Testing correlations for slug frequency

The two-phase experimental data is compared with some of the correlations existing in the literature and listed in Table 1. Fig. 9 shows the performance of nine correlations that give better predictions from Table 1. It can be noted that different correlations provide very different results. Some correlations underestimate the present measurements of the slug frequency, while others predict larger values.

Table 3 shows four statistical parameters, mean squared error (MSE), averaged percentage difference (APD), averaged absolute percentage difference (AAPD) and root mean squared percentage difference (RMSPD), between the measured frequency and the predicted values of frequency from the different correlations, these parameters are calculated using Eqs. (5) to (7). The best prediction is obtained with the correlation proposed by Thaker and Banerjee (2016b), which relates the mixture Strouhal number (St_M) with the input liquid fraction λ_f. Moreover, with he exception of the correlation by Fetter (1988), the best predictions are generally obtained with the correlations based on the Strouhal number (gas or mixture based), these are marked with an asterix in Table 3.

$$APD = \frac{1}{n}\sum_{k=1}^{n}\left[\frac{f_{S,pred} - f_{S,exp}}{f_{S,exp}}\right] \times 100 \tag{5}$$

$$AAPD = \frac{1}{n}\sum_{k=1}^{n}\left|\frac{f_{S,pred} - f_{S,exp}}{f_{S,exp}}\right| \times 100 \tag{6}$$

$$RMSPD = \sqrt{\frac{1}{n}\sum_{k=1}^{n}\left[\frac{f_{S,pred} - f_{S,exp}}{f_{S,exp}}\right]^2} \times 100 \tag{7}$$

When plotting the Strouhal number (gas or mixture based) against the gas or liquid input fractions, it can be seen that the data collapse into specific curves. In Fig. 10 the mean frequencies are fitted to curves involving different definitions of the Strouhal number and the input fraction. The fitting was performed globally, this is for all the data together, and separately for plug-to-slug transition flow and slug flow regimes, as proposed by Arabi et al. (2020b), which leads to better approximations. The error bars are calculated with error propagation using the standard deviation of the Poisson distribution

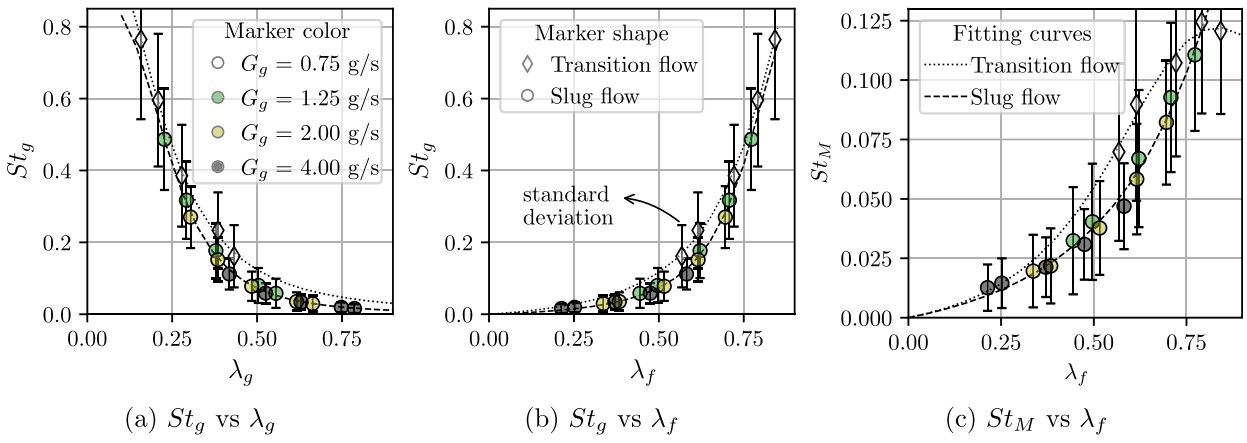

Fig. 10. Two-phase data collapsed in curves of non-dimensional parameters. (For interpretation of the references to color in this figure legend, the reader is referred to the web version of this article.)

Table 3
Performance of previous correlations with the experimental data.

Correlation	MSE	APD	AAPD	RMSPD
Gregory and Scott (1969)	13.8	−41.7	41.7	44.7
Fetter (1988)	3.88	−6.49	20.0	22.9
Manolis et al. (1995)	3.15	32.9	33.0	40.0
Fossa et al. (2003)*	2.73	−16.7	18.1	22.3
Wang et al. (2007)*	8.99	−21.5	26.3	33.0
Thaker and Banerjee (2015)	15.2	91.0	91.0	106.9
Thaker and Banerjee (2016b)*	2.17	−10.8	16.2	19.2
Al-Safran (2016)	10.3	−29.6	30.6	36.4
Arabi et al. (2020a)*	6.72	−27.6	27.6	31.6

of the frequency (Fig. 5) and the instrumentation uncertainties. The parameters and the fitting equations are indicated in Table 4. The performance of the fitted correlations is evaluated with the values of MSE, APD, AAPD and RMSPD. It can be seen that all the three correlations perform very well and that separating the flow regimes yields to better approximations. Yet, a slight improvement is achieved when calculating the gas Strouhal number (St_g) as a function of the gas or liquid input fraction (λ_g or λ_f) Figs. 11a and 11b, respectively.

Furthermore, a linear relationship was observed by Arabi et al. (2020b) when plotting the gas based Strouhal number against the Lockhart–Martinelli parameter (X_{LM}), using data from different authors. This parameter was proposed by Lockhart and Martinelli (1949) for analyzing two-phase flows and is defined in Eq. (8), where $(\delta P/\delta z)_g$ and $(\delta P/\delta z)_f$ are the gas and liquid frictional pressure gradients, respectively. In Fig. 11 a linear fitting between St_g and X_{LM} is shown in red for two- and three-phase runs. For three-phase flows the slurry friction gradient $(\delta P/\delta z)_{fs}$ is used instead of the liquid one Eq. (9). Further details on calculating X^*_{LM} can be found in Sassi et al. (2020b).

$$X_{LM} = \sqrt{\frac{\left(\delta P/\delta z\right)_f}{\left(\delta P/\delta z\right)_g}} \tag{8}$$

$$X^*_{LM} = \sqrt{\frac{\left(\delta P/\delta z\right)_{fs}}{\left(\delta P/\delta z\right)_g}} \tag{9}$$

The data collapse quite well in the linear fitting. However, a strong deviation towards the origin is observed for runs with low values of liquid superficial velocities and high values of gas superficial velocities. Low impact of the solid phase is found in the slope of the linear fitting, with values of 0.0125, 0.0129 and 0.0130 for two-phase flow, three-phase flow with $C_S = 10\%$ and $C_S = 20\%$, respectively. However, better predictions can be obtained using an asymptotic curve as correlation. The black dashed lines correspond to fitting the data to Eq. (10), where a, b and c are the fitting parameters. Note that in the case of three-phase flows the modified Lockhart–Martinelli is used. In Table 5 the fitting parameters are presented for two- and three-phase flows together with the statistical parameters.

$$St_g = \frac{a \cdot X_{LM}^b}{X_{LM} + c} \tag{10}$$

3.2. Bubble velocity

Mean bubble velocity (V_t) is calculated by averaging the nose and tail velocities of all bubbles recorded by the camera during the 17 s. The displacement of the noses and tails was computed using the cross-correlation of two subsequent frames, following a similar technique as the conventional Particle Image Velocimetry (PIV). The details of this procedure is described in Appendix B.2. In Fig. 12 the mean velocities of the bubbles are plotted for the different two-phase runs versus the superficial mixture velocity (j_M). The colors of the markers indicate the gas mass flow, and the error bars represent the standard deviation of the samples. The number of bubbles visible in the time window (17 seconds) has been indicated with the size of the markers of Fig. 12.

Fig. 12 shows that as j_M increases, the average velocity of the bubbles increases linearly with a slope of about 1.1 with the superficial mixture velocity, as indicated by the dashed line in Fig. 12. The red and green dotted lines represent the models to correlate the bubble translational velocity with the mixture velocity found by Thaker and Banerjee (2016b) (Eqs. (11) and (12)) and Xu et al. (2020) (Eq. (13)), respectively. It can be seen that Thaker and Banerjee's model approximates better to the experimental data, specially for the first segment ($Fr \leq 3.5$) which corresponds to mixture velocities under 1.9 m/s. Also, the variability of the bubble velocity increases at higher j_M, as shown by larger standard deviations (Thaker and Banerjee, 2016b). Equivalent plots are presented for three-phase flows in Figs. 13a and 13b for 10% and 20% of solid loading, respectively.

$$V_t = 1.005 \cdot j_M + 0.19 \quad \text{for} \quad Fr \leq 3.5 \tag{11}$$

$$V_t = 1.1916 \cdot j_M \quad \text{for} \quad Fr \geq 3.5 \tag{12}$$

$$V_t = 1.218 \cdot j_M + 0.142 \quad \text{for} \quad j_M \leq 6 \text{ m/s} \tag{13}$$

From Figs. 12 and 13 it can be seen that three-phase flows exhibit a larger dispersion of the bubble velocity. In two-phase flows (Fig. 12), the bubble velocity is mainly between 1 and 1.1 times the mixture velocity. In the case of three-phase flows (Fig. 13), the bubble velocity ranges from 1 up to 1.5 times the mixture velocity. In Fig. 13a the dashed lines represent slopes of 1.1 and 1.5, and in Fig. 13b the indicated slope is 1.25.

Table 4
Performance of the fitted correlations from Fig. 10.

Correlation	$St_g(\lambda_g)$			$St_g(\lambda_f)$			$St_M(\lambda_f)$		
Equation	$St_g = \frac{A}{1+B\lambda_g^C}$			$St_g = \frac{A\lambda_f}{1+B\lambda_f+C\lambda_f^2}$			$St_M = \frac{A\lambda_f}{1+B\lambda_f+C\lambda_f^2}$		
Fitted parameters	trans (⋄)	slug (o)	global (⋄ + o)	trans (⋄)	slug (o)	global (⋄ + o)	trans (⋄)	slug (o)	global (⋄ + o)
A	1.07	0.874	0.99	0.065	0.032	0.038	0.032	0.031	0.023
B	45.2	111.7	96.93	−1.94	−2.171	−2.13	−2.14	−1.469	−2.07
C	2.560	3.336	3.140	0.995	1.222	1.178	1.440	0.586	1.267
MSE	0.040	0.078	0.47	0.041	0.115	0.45	0.057	0.132	0.52
APD	0.227	1.034	8.19	0.072	−3.921	2.43	0.182	−2.157	−1.83
AAPD	3.305	5.358	14.19	3.152	8.286	10.61	3.348	8.247	12.38
RMSPD	4.162	6.301	17.67	3.807	10.982	13.35	3.565	10.444	16.11

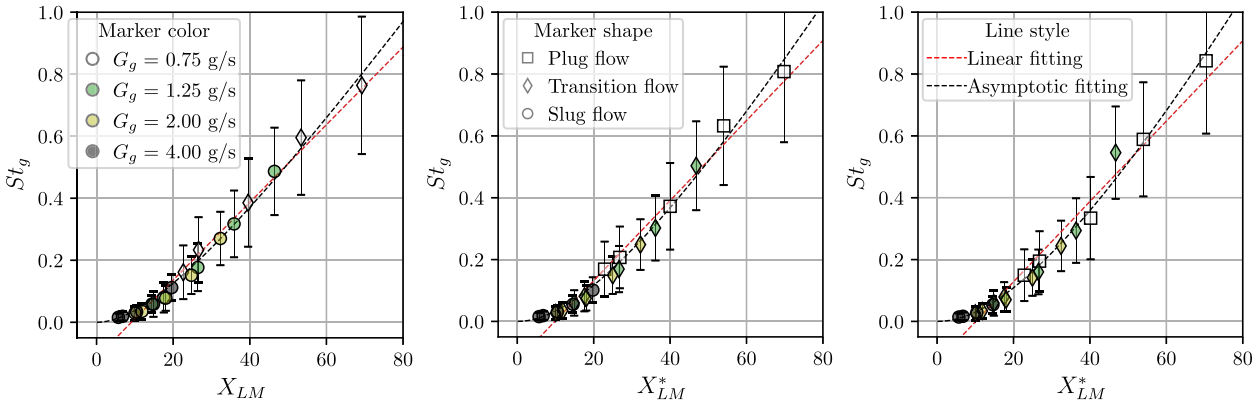

Fig. 11. Gas based Strouhal number versus Lockhart–Martinelli parameter for two- and three-phase flow. (For interpretation of the references to color in this figure legend, the reader is referred to the web version of this article.)

Table 5
Performance of the fitted correlations from Fig. 11.

Fitted parameters	Two-phase flow	Three-phase flow	
		$C_S = 10\%$	$C_S = 20\%$
a	0.018	0.015	0.012
b	2.0	2.0	2.1
c	37.0	40.4	41.9
APD	10.6	6.4	3.6
AAPD	16.0	14.4	11.9
RMSPD	20.8	17.0	14.4

A more detailed analysis of the bubble velocities is given in Fig. 14 for two-phase flows. This figure shows the effect of the liquid superficial velocity and the air mass flow rate on the bubbles mean velocity (Fig. 14a), the nose and tail of velocities (Figs. 14b and 14d) and the standard deviation (Fig. 14c). Again, the colors of the symbols indicate the mass flow rate of air. Note that the gas velocity differs along runs with the same mass flow, because of the increment of pressure related to an increasing liquid superficial velocity. The mean bubble velocity (Fig. 14a) is the average between the velocities of the nose (Fig. 14b) and the tail (Fig. 14d). As expected, by increasing any of both, liquid or gas flow rate, the velocity of the bubbles also increases. However, for high air flow rates (black dots), the increment of the bubble velocity due to increasing j_f is not as strong as in the other runs.

Figs. 14b and 14d show the nose and tail mean velocities respectively. The comparison of these two figures shows that the slope of the nose mean velocity is steeper than the slope of the tail velocity, and the symbols corresponding to the different gas mass flow rates are closer in the nose velocity and further distant to each other on the tail graph. This means that the liquid superficial velocity has greater impact on the nose velocity than it has on the tail velocity, while the gas

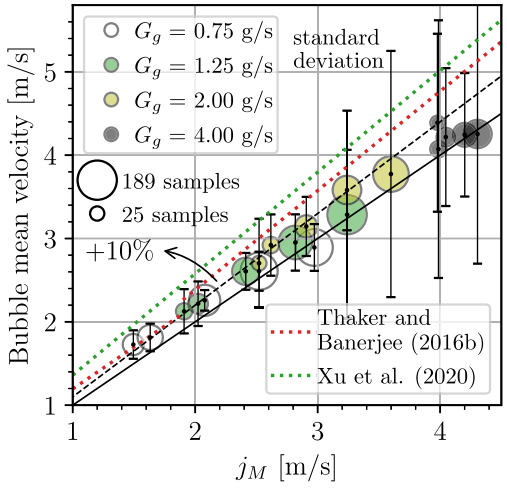

Fig. 12. Bubble mean velocity per run vs. mixture velocity for two-phase flow. Color indicates gas mass flow rate, the size of the symbol indicates the number of bubbles and the error bars indicate the standard deviation. (For interpretation of the references to color in this figure legend, the reader is referred to the web version of this article.)

superficial velocity has a greater influence over the tail velocity. Also, it can be noted that for higher rates of air, the upward trend in bubble velocity is inverted in the zone of low liquid superficial velocities. Similar conclusions were found in Thaker and Banerjee (2016a,b).

In addition, it can be seen that the tail velocity highly increases for higher air mass flow rates. The white markers (low air rates) in Figs. 14b and 14d are at comparable levels, but at higher air rates the tail velocity becomes larger than the nose velocity for a constant

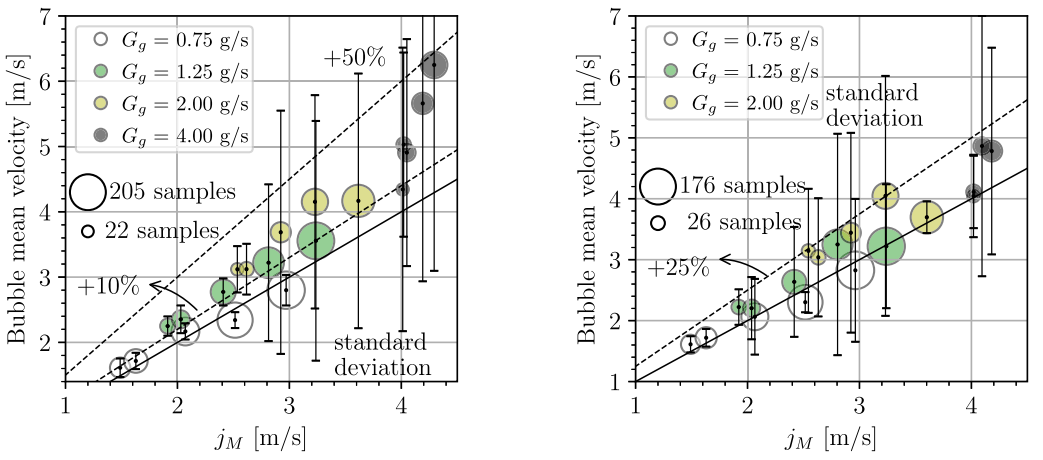

(a) 10% loading. (b) 20% loading.

Fig. 13. Bubbles mean velocity per run vs. mixture velocity for three-phase flow. Color indicate gas mass flow rate, the size of the symbol indicates the number of bubbles and the error bars indicate the standard deviation. (For interpretation of the references to color in this figure legend, the reader is referred to the web version of this article.)

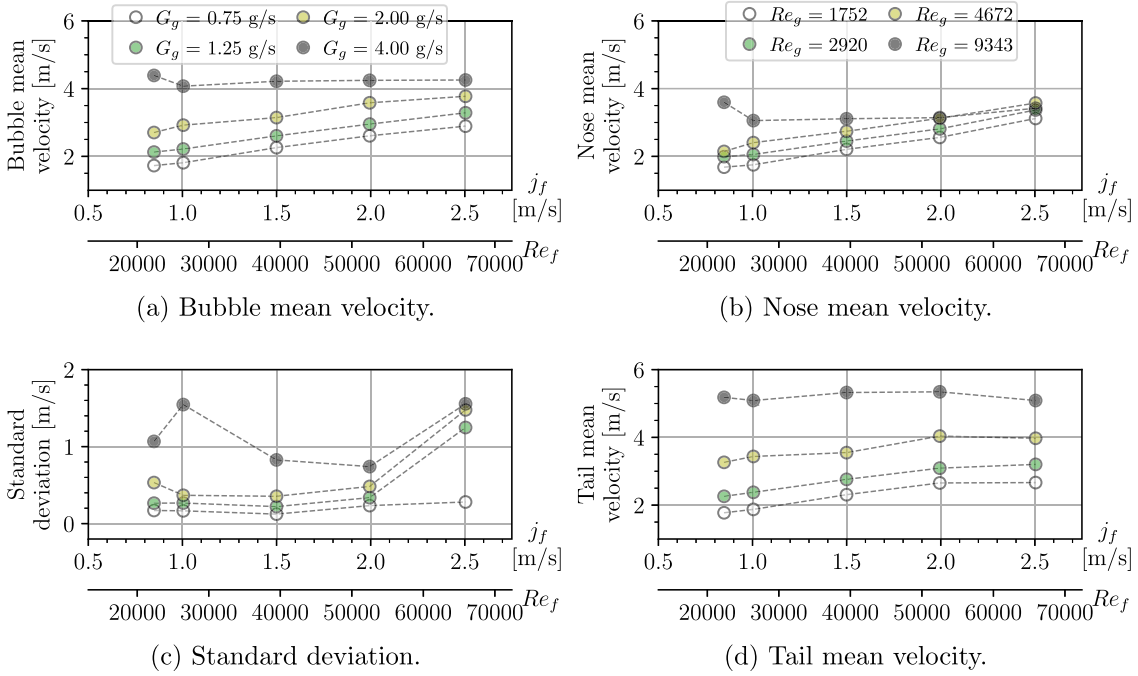

(a) Bubble mean velocity. (b) Nose mean velocity.

(c) Standard deviation. (d) Tail mean velocity.

Fig. 14. Incidence of liquid superficial velocity and gas mass flow rate on bubbles velocity in two-phase flow. (For interpretation of the references to color in this figure legend, the reader is referred to the web version of this article.)

liquid superficial velocity. For regimes with high air flow rates, aeration in front of liquid pockets increases along with turbulence. This high aeration near the tail of the bubble, together with the overcoming of the liquid film underneath the bubble (which moves much slower than the bubble and the liquid pocket), produces strong eddies in the tail of the bubble which in turn generate the effect of a wave breaking at the tail of the bubble (Sassi et al., 2020b), thus increasing the tail velocity.

In Fig. 15 the same analysis is presented for three-phase flows with 10% of solid loading. In general, a similar behavior is observed between two-phase and three-phase runs. For the mean velocity, very similar values and trends are obtained for the lower air flow rates. However for the gray dots (4.0 g/s of air) in two-phase flow (Fig. 14a) the influence of the liquid superficial velocity is smaller, while for three-phase flows a similar trend is observed for the four air mass flow rates (Fig. 15a). For the nose velocity, similar slopes are identified, which indicate that the effect that induces the liquid superficial velocity is very similar in both cases. On the other hand, the effect of the air flow rate is more significant for three-phase flows, as the markers are more spread apart in the vertical direction. Looking at the tail velocities in Figs. 14d and 15d very similar values are observed for all the runs. Finally, when comparing the standard deviations of the mean velocity in Figs. 14c and 15c, an increase of the variation is obtained for the three-phase runs. At low values of superficial velocities the standard deviation value are similar, but a strong increment is noted for increasing superficial velocities.

To conclude with the bubble velocity analysis, results are presented for the 19 runs of three-phase flows with 20% of solid concentration in Fig. 16. The mean results are very similar to those corresponding to 10% of solid concentration shown in Fig. 15. The main difference is observed in the standard deviations, which increase in value from even lower superficial velocities values both of water and air.

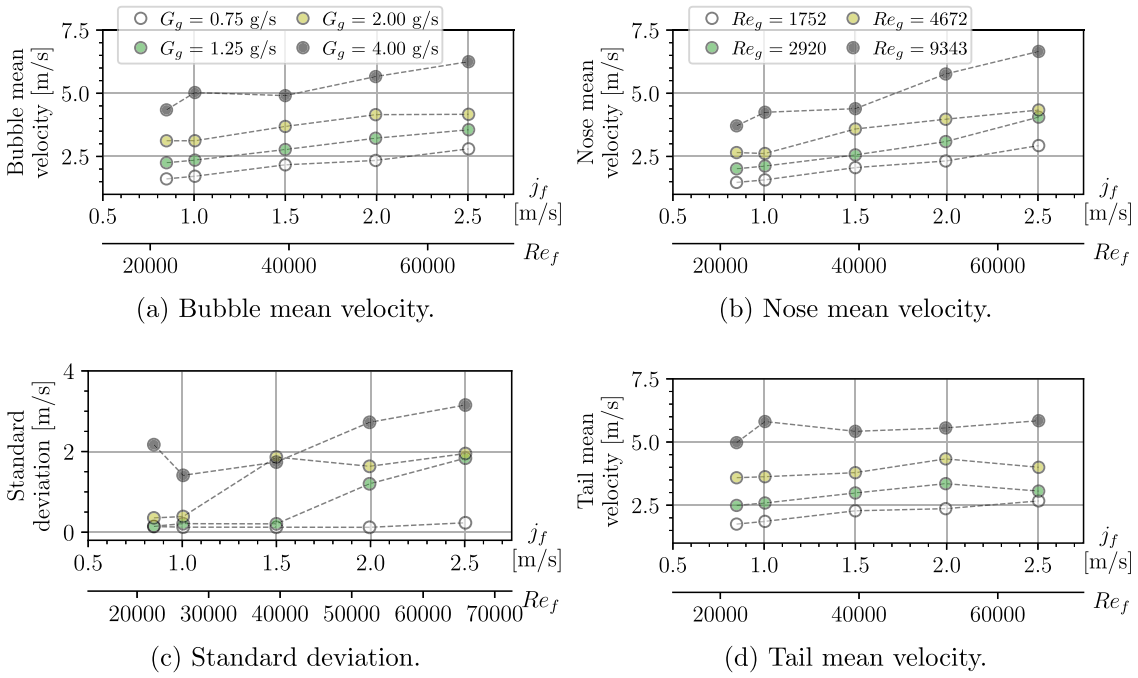

(a) Bubble mean velocity. (b) Nose mean velocity.

(c) Standard deviation. (d) Tail mean velocity.

Fig. 15. Effect of the liquid superficial velocity and gas mass flow rate on the bubble velocities for three-phase flow with 10% of solid concentration.

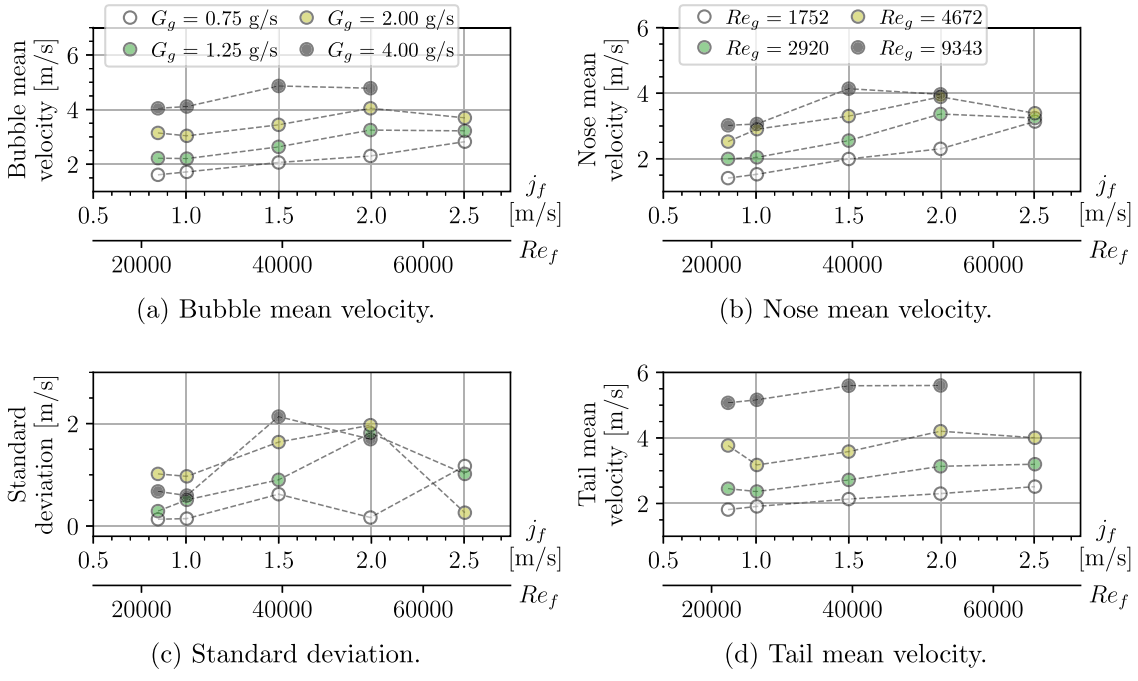

(a) Bubble mean velocity. (b) Nose mean velocity.

(c) Standard deviation. (d) Tail mean velocity.

Fig. 16. Effect of the liquid superficial velocity and gas mass flow rate on the bubble velocities for three-phase flow with 20% of solid concentration.

3.3. Bubble length

Finally, the length of the bubbles is determined from Eq. (14), using the mean velocity of each bubble ($\bar{U}_b$) and the residence time of the corresponding bubble in the cross section ($t_1 - t_0$) of the line-scan image. In Eq. (14) t_0 is the time at which the nose intersects the monitored cross section, and t_1 is the time at which the tail passes through the monitored cross section. The time difference ($t_1 - t_0$) corresponds to the distance in pixels between a blue line and the consecutive red line in the line-scan image (Fig. 4) divided by the frame rate. The results are presented in Fig. 17 for two and three phase flows. The dashed lines are linear fittings for operating condition with the same liquid superficial velocities. The slopes of the linear fittings are presented in Table 6.

$$L_b = \bar{U}_b \cdot (t_1 - t_0) \tag{14}$$

It can be seen that in general the length of the bubbles is increased due to the presence of the solid phase, since lines with larger slopes are obtained for increasing solid concentrations. This is in concordance with the decrease of the slug frequency, since longer bubbles with the same mixture velocity have longer residence times and therefore smaller frequencies. This is explained for the accumulation of solid particles at the interface in the tail of the bubbles, that avoids the

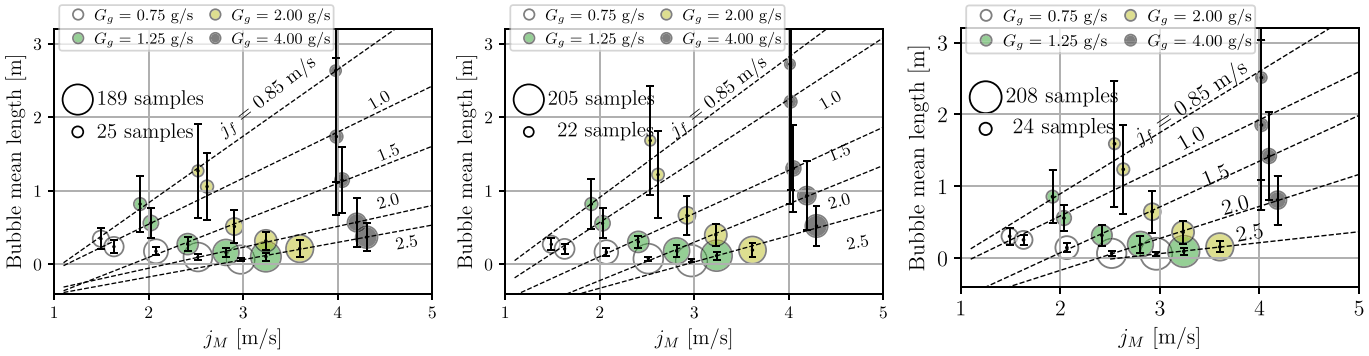

(a) Two-phase flow. (b) Three-phase flow, C_S = 10%. (c) Three-phase flow, C_S = 20%.

Fig. 17. Bubbles mean length vs. mixture velocity.

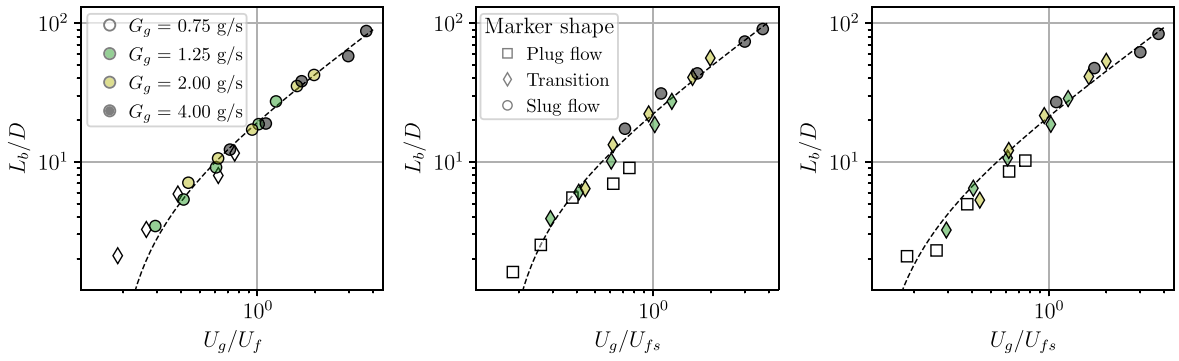

(a) Two-phase flow. (b) Three-phase flow, C_S = 10%. (c) Three-phase flow, C_S = 20%.

Fig. 18. Dimensionless bubble length vs. gas-to-liquid superficial velocity ratio. (For interpretation of the references to color in this figure legend, the reader is referred to the web version of this article.)

Table 6
Slopes of linear fittings between bubble mean length and mixture velocity.

j_f [m/s]	2-Phase	3P-10%	3P-20%
0.85	0.906	0.955	0.851
1.00	0.627	0.837	0.668
1.50	0.504	0.587	0.637
2.00	0.285	0.522	0.445
2.50	0.235	0.357	0.152[a]

[a]Only 3 points are used for linear fitting.

Table 7
Fitted parameters for elongated bubble length linear correlation.

Fitted parameters	Two-phase flow	Three-phase flow	
		C_S = 10%	C_S = 20%
a	23.5	26.5	24.1
b	−4.25	−4.4	−3.0

detachment of small bubbles and thus, longer bubbles are obtained for the same values of liquid and gas flow rates. Finally, it can be seen that the standard deviations of the bubble mean length (indicated with the error bars in Fig. 17) increase with both liquid and gas flow rates.

Further, the dimensionless bubble length (L_b/D) can be represented as a function of the gas-to-liquid superficial velocity, as recommended by Arabi et al. (2021), for two-phase flows. Fig. 18 shows how the data collapse into a straight line for two and three phase flows in logarithmic scale. Note that for three phase flows the slurry superficial velocity (U_{fs}) is used instead of U_f. The dashed lines correspond to fitting the data to straight lines. The fitting parameters are listed in Table 7.

Finally the correlations of Thaker and Banerjee (2016b) (Eq. (15)) and Wang et al. (2007) (Eq. (16)) are tested with our data in Fig. 19 with black and green markers, respectively.

$$\frac{L_b}{D} = 1.22 \times 10^3 (Re_f)^{-1.27} (Re_g)^{1.2} \tag{15}$$

$$\frac{L_b}{D} = 12.07 (U_f^*)^{-1.67} (U_g^*)^{1.14}, \quad U_f^* = \frac{U_f}{\sqrt{gD(1-\rho_g/\rho_f)}} \tag{16}$$

The parameters from Thaker and Banerjee (2016b) correlation have been fitted to our data and are plotted with red markers. The yellow markers correspond to the linear modeling from Fig. 18. Good predictions are obtained with Thaker and Banerjee (2016b) correlation while Wang et al. (2007) correlation underestimates the bubble length. The linear fitting with the gas-to-liquid superficial velocity ratio also provides good predictions of the bubble length. Statistic parameters for the tested correlations are presented in Table 8.

4. Conclusions

In this study, slug frequency was experimentally analyzed for intermittent two-phase flows. Moreover, the influence of solid particles on the slug frequency was investigated.

Several measurement techniques were tested and compared. The Wilkens and Thomas method, with pressure taps spacing of 25 and 50 cm and a sampling rate of 50 Hz showed that a higher sampling rate and low-noise signals are required in order to obtain reliable measurements of the slug frequency. Power spectral densities were calculated for differential pressure signals and for mean intensity signals of the line-scan images. In general, power spectral densities provide useful information, since it identifies the frequencies involved in the motion of the intermittent flows. However, it is not a suitable method for calculating mean frequencies, as it is necessary to deeply analyze

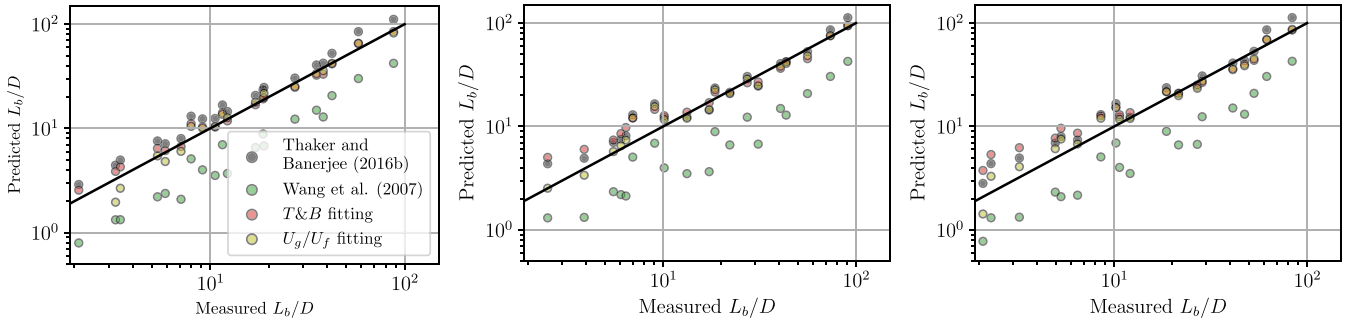

(a) Two-phase flow. (b) Three-phase flow, $C_S = 10\%$. (c) Three-phase flow, $C_S = 20\%$.

Fig. 19. Tested correlations for modeling the elongated bubble length. (For interpretation of the references to color in this figure legend, the reader is referred to the web version of this article.)

Table 8
Performance of the fitted correlations from Fig. 19.

Correlation	Statistic parameters	Two-phase flow	Three-phase flow $C_S = 10\%$	Three-phase flow $C_S = 20\%$
Thaker and Banerjee (2016b)	APD	29.2	23.4	26.7
	AAPD	29.2	29.3	29.0
	RMSPD	32.4	39.8	38.0
Thaker and Banerjee (2016b) (fitted)	APD	6.7	26.8	30.3
	AAPD	11.5	32.2	37.1
	RMSPD	15.1	46.9	51.5
Wang et al. (2007)	APD	−57.5	−59.1	−57.9
	AAPD	57.5	59.1	57.9
	RMSPD	58.1	60.7	58.9
$\frac{L_b}{D} = a\frac{U_g}{U_f} + b$ (parameters in Table 7)	APD	−5.7	3.4	9.0
	AAPD	15.9	19.0	19.9
	RMSPD	25.8	29.4	24.7

individually each spectrum. In some cases the mean frequency matches the main frequency from the PSD, but in general several peaks with similar values are obtained for several values of frequency and therefore, it is recommended to use it together with other measurement techniques in order to fully characterize the motion. The measurement of the frequency from the line-scan images, results in the distribution of frequencies of the motion of intermittent flows.

Measurements of slug frequency with image processing of the line-scan images were presented for 59 different operating conditions including mean frequencies and histograms of two and three-phase flows. The presented data are valuable for developing and testing of computational fluid dynamics models. Two-phase flow slug frequencies were measured, and correlations within the available literature were tested. A wide spectrum of behaviors were found, where some correlations overestimate significantly the slug frequency while others underestimate it. Good predictions were obtained with the Thaker and Banerjee correlation, which relates the mixture based Strouhal number (St_M) to the input liquid fraction λ_f. However, when trying to fit the experimental data to collapsing curves, the best performance was found when relating the gas based Strouhal number (St_g) with the input fractions (λ_g and λ_f). Finally, it was found that increasing the solid concentration induces a slight decrease in slug frequency. This could be explained by the accumulation of solid particles in the tail of the elongated bubbles that avoids the detachment of bubbles.

When correlating the gas based Strouhal number as a function of the Lockhart–Martinelli (X_{LM}), the experimental data collapse quite well in a straight line, as observed by Arabi et al. (2020b). However, a better fitting is found for our data with asymptotic curves. Very similar results are found for three-phase flows using the modified Lockhart–Martinelli parameter (X^*_{LM}), which indicates that the correlation may be used both for two- and three-phase flows.

Measurements of nose and tail mean velocities have been presented for all operating conditions. Similar trends are found for the liquid superficial velocity. However, the effect of the gas mass rate is more significant in three-phase flows, specially in the nose velocity. Also, a greater variability on the velocities are found for increasing solid concentrations. Finally, bubble length measurements have shown that the increase of the solid concentration increases the length of the elongated bubbles. Therefore, this can also be attributed to the effect of the accumulation of solid particles near the tail of the elongated bubbles. Correlations were tested for modeling the bubble length, the linear relationship between the dimensionless bubble length and the gas-to-liquid superficial velocity ratio results a very simple correlation that performed very well.

Declaration of competing interest

The authors declare that they have no known competing financial interests or personal relationships that could have appeared to influence the work reported in this paper.

Acknowledgments

This project has received funding from the European Union's Horizon 2020 research and innovation programme under the Marie Sklodowska-Curie grant agreement No. 713679; from the Spanish government under the grants DPI2016-75791-C2-1-P and PID2020-113303GB-C21; and from Generalitat de Catalunya under grant 2017-SGR-01234. These supports are gratefully acknowledged. We thank Repsol for providing the polypropylene pellets for the three-phase experiments.

Appendix A. Pressure measurements

Three measurements of differential pressure have been performed for each run, $\Delta P_{12} = PT_1 - PT_2$, $\Delta P_{23} = PT_2 - PT_3$ and $\Delta P_{3o} = PT_3 - P_{atm}$, comprising the pressure taps PT_1, PT_2 and PT_3 shown in Fig. 2. Before taking measurements, each regime was allowed to reach its stationary state for at least two minutes. Then, each of the 3 pressure measurements have been recorded for 2 min with a sample rate of 50 Hz. As an example, Fig. A.20 shows 5 seconds of the pressure signals obtained for a two-phase run with $j_g = 1.61$ and $j_f = 1.0$ m/s.

The slug frequency can be obtained from the above pressure measurements using counting peaks methods. In this way, a mean frequency can be obtained. On the other hand, the power spectral density can be calculated in order to obtain the main slug frequencies of the motion.

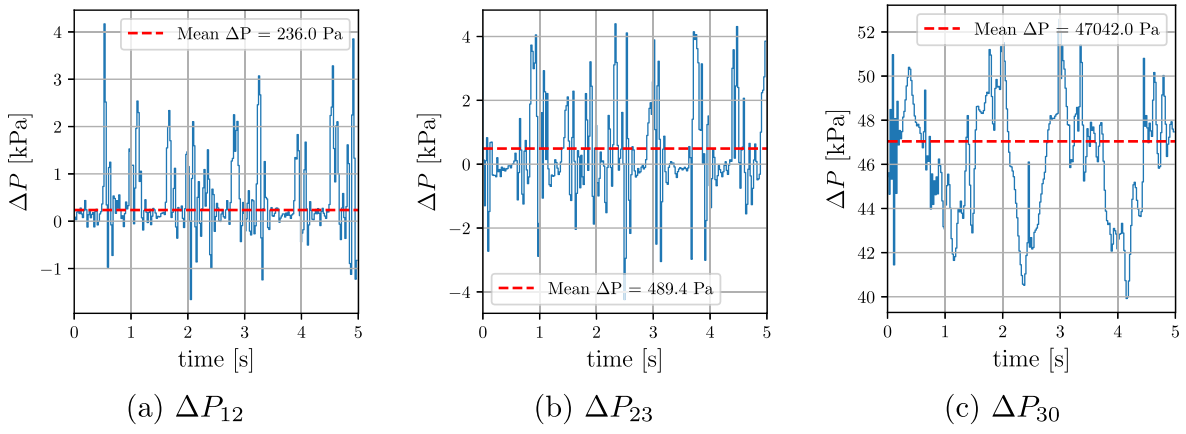

Fig. A.20. Example of independent pressure measurements during 5 s, (a) $\Delta P_{12} = P_1 - P_2$, (b) $\Delta P_{23} = P_2 - P_3$ and (c) $\Delta P_{3o} = P_3 - P_{atm}$. Two-phase run with $j_f = 1.0$ m/s and $j_g = 1.61$ m/s.

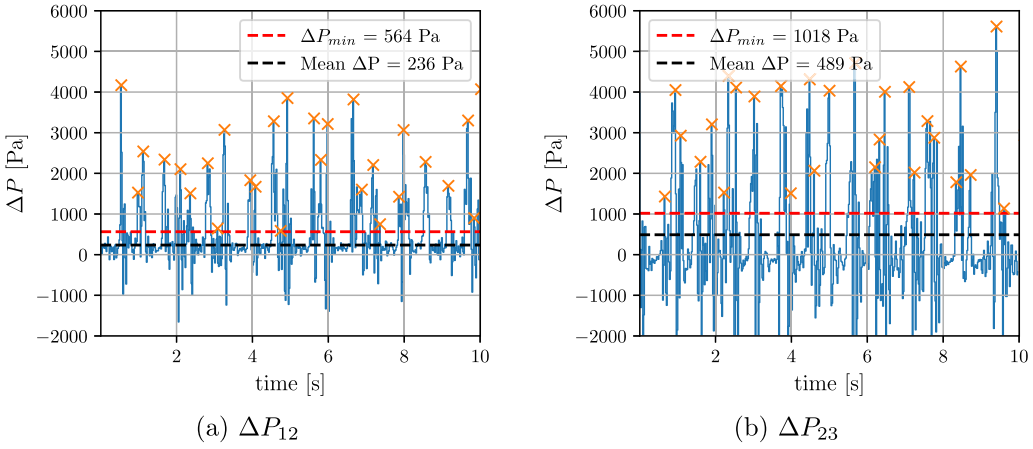

Fig. A.21. Example of the Wilkens & Thomas method, counting peaks during 10 s of two-phase flow with $j_f = 1.0$ m/s and $j_g = 1.02$ m/s. Pressure taps spacing (a) 25 cm and (b) 50 cm.

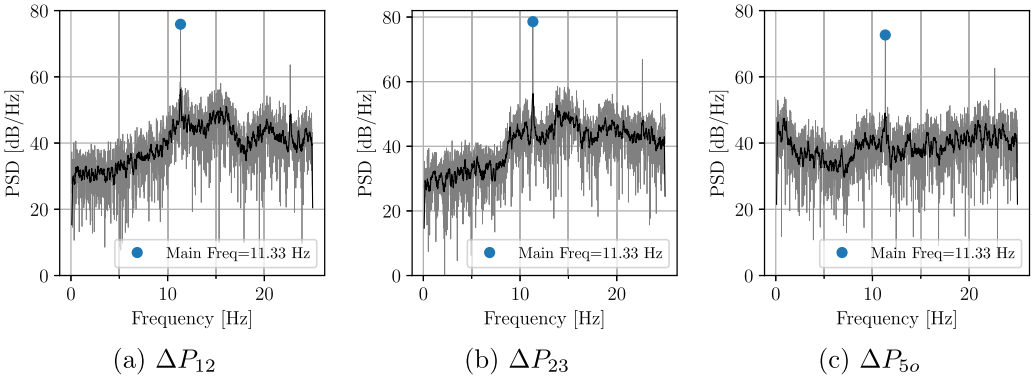

Fig. A.22. Example of power spectral densities, two-phase flow with $j_f = 2.5$ m/s and $j_g = 0.47$ m/s. Differential pressure with taps spacing (a) 25 and (b) 50 cm. And (c) gauge pressure at tap PT3.

A.1. Wilkens & Thomas method

The Wilkens & Thomas method (Wilkens and Thomas, 2008) is based on counting the peaks that reach a certain threshold, on a signal obtained from a differential pressure measurement between two pressure taps. These authors considered that the transit of a liquid pocket between the two taps would produce a greater pressure loss than the presence of an elongated bubble. The method can be summarized in the following steps:

- Consider the liquid pocket velocity as the mixture velocity,

$$U_{lp} = j_M = j_f + j_g \tag{A.1}$$

- Calculate the friction factor of the liquid pocket using the Reynolds number based on the liquid pocket velocity, the diameter of the pipe and the liquid viscosity,

$$\mathrm{f} = 0.0014 + \frac{.125}{Re_{lp}^{0.32}} \tag{A.2}$$

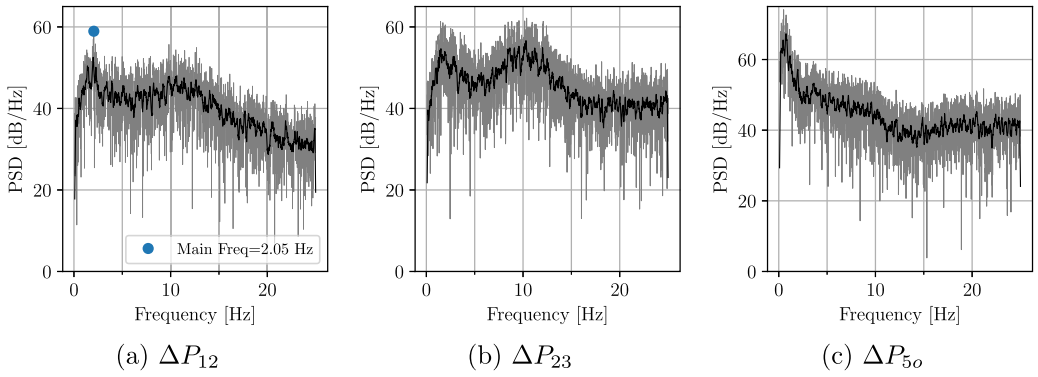

Fig. A.23. Example of power spectral densities, two-phase flow with $j_f = 1.0$ m/s and $j_g = 1.02$ m/s. Differential pressure with taps spacing (a) 25 and (b) 50 cm. And (c) gauge pressure at tap PT3.

- Estimation of the minimum stable slug length,

$$L_{min} \geq D \cdot (10 j_f + 5) \tag{A.3}$$

- Estimation of the minimum pressure drop due to the skin friction of a liquid pocket,

$$\Delta P_{min} = 2\mathrm{f} \cdot \frac{L_{min} \rho_f V_{lp}^2}{D} \tag{A.4}$$

Note that if the liquid pocket is longer than the distance between the pressure taps, the length used to predict the pressure drop should be constrained to the taps distance. Then, the method consists in counting peaks above the ΔP_{min} threshold, and the mean frequency is deduced from Eq. (A.5),

$$f_s = \frac{N_{peaks}}{\Delta t} \tag{A.5}$$

where N_{peaks} is the number of peaks exceeding the threshold and Δt the time interval. Fig. A.21 shows examples of the application of the Wilkens & Thomas method to the signals shown in Figs. A.20a and A.20b. Note that the method is only applicable to differential pressure measurements.

In Fig. A.21a the minimum stable liquid pocket length is constrained to the taps spacing (25 cm) and the obtained threshold is 564 Pa. While in Fig. A.21b the minimum stable length (45.1 cm) is smaller than the spacing (50 cm), and thus no constraint is applied in obtaining the threshold of 1018 Pa.

A.2. Power spectral density

The power spectral density (PSD) represents the energy distribution of a time signal along the frequency components of the signal. It is a very useful tool to characterize random variables of stochastic processes. Here the PSD is used to determine the main slug frequencies from pressure signals over time. Fig. A.22 shows three PSD calculated for the pressure signals of a two-phase flow with $j_f = 2.5$ m/s and $j_g = 0.47$ m/s.

For this regime, that corresponds to a relatively high liquid superficial velocity and low gas velocity, a very large peak is obtained at a frequency of 11.33 Hz for the three pressure measurements. So it is easy to determine the main frequency of slugs. A lower peak, at twice the main frequency is also observed, which corresponds to the presence of harmonics.

Other flow regimes do not show a clear main frequency, as is the case for the pressure measurements from Fig. A.23 with $j_f = 1.0$ m/s and $j_g = 1.02$ m/s. The lack of a noticeably protruding peak characterizes these flow regimes, and instead many peaks of similar power are seen for a wide range of frequencies. It should be noted that the application of low pass filters to the signal needs care because the selection of a frequency for the filter can hide natural slug frequencies.

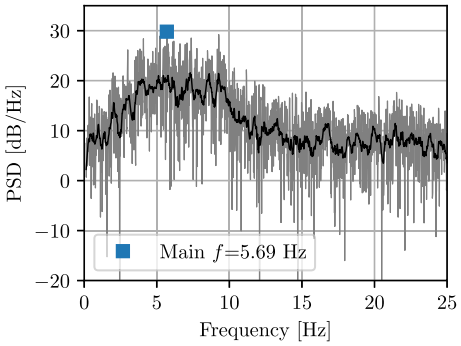

Fig. B.24. Power spectral density of a mean intensity signal from a line-scan image, two-phase flow $j_f = 2.5$ m/s and $j_g = 0.58$ m/s.

Appendix B. Image processing

Two different types of images were taken for each flow regime. One for the analysis of the slug frequency, and the other to determine the size and the velocity of the elongated bubbles. The processing techniques used for these two types of images are described below.

B.1. Frequency analysis

The slug frequency is measured with an image processing technique using images from the fast camera. For this, images were captured in the test section, 150 D downstream the mixing chamber, at 3200 frames per second with a resolution of 1 × 640 pixels in the axial and vertical directions respectively. For each run, 75 s of images were taken, corresponding to a total of 240,000 frames per run. Each image has been pre-processed with background subtraction and histogram stretching to enhance contrast. A line-scan image is obtained by placing one column of pixels from every pre-processed image next-to each other. In this way, a 240,000 × 640 pixels image is obtained, a section of the image is showed in Fig. 4a. The vertical coordinate of the resulting image corresponds to the vertical axis of the pipe, and the horizontal axis is the evolution in time of the flow state as it passes through the selected cross section (during 75 s).

Finally, the frequency can also be estimated by calculating the PSD of the mean intensity signal of a line-scan image, plotted in the bottom panel of Fig. 4. This is a much faster way to determine the dominant frequency, as the only processing required is calculating the signal and its PSD, without using the bubble location algorithm. Fig. B.24 shows an example of applying the PSD to the mean intensity signal from Fig. 4b.

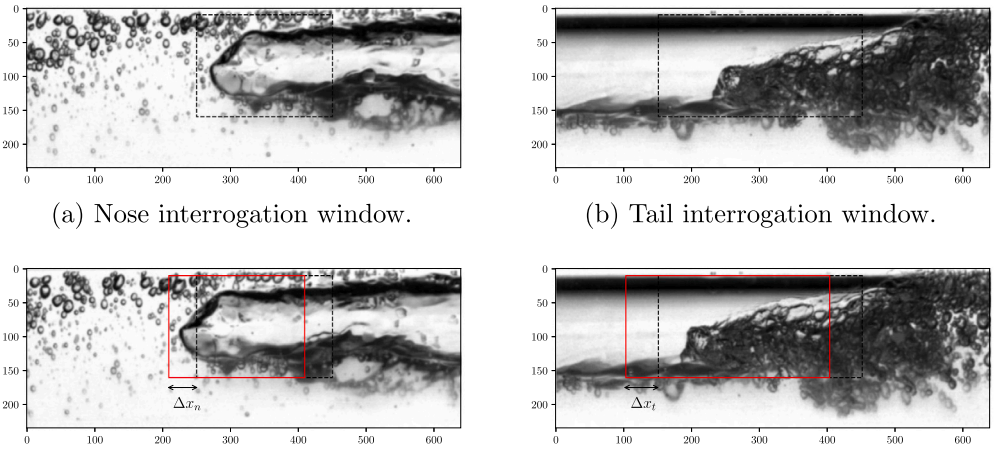

(a) Nose interrogation window. (b) Tail interrogation window.

(c) Maximum correlation coefficient location at tenth following frame. (d) Maximum correlation coefficient location at tenth following frame.

Fig. B.25. Example of cross-correlation applied to nose and tail of an elongated bubble to calculate velocity and size of bubble. Two-phase run with $j_f = 1.0$ m/s and $j_g = 1.02$ m/s, flowing from right to left. (For interpretation of the references to color in this figure legend, the reader is referred to the web version of this article.)

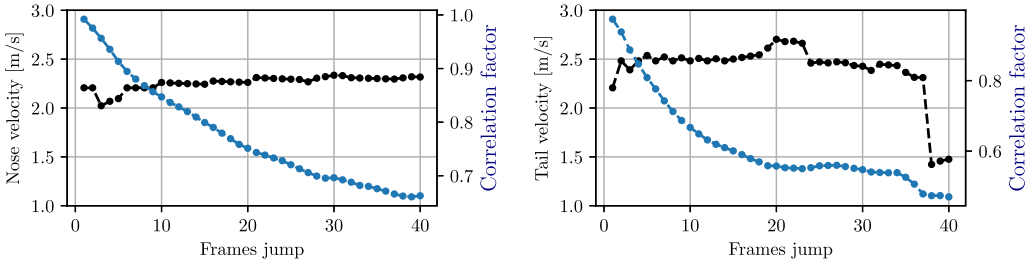

(a) Nose velocity. (b) Tail velocity.

Fig. B.26. Sensitivity analysis of velocity calculation with cross-correlation between image n and $n + jump$. Two-phase run with $j_f = 1.0$ m/s and $j_g = 1.02$ m/s (same bubble than Fig. B.25). (For interpretation of the references to color in this figure legend, the reader is referred to the web version of this article.)

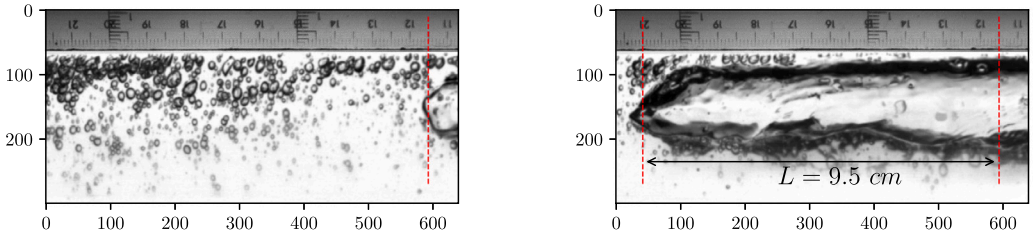

(a) (b)

Fig. B.27. Pixel calibration and pixel size measurement. Two-phase run with $j_f = 1.0$ m/s and $j_g = 1.02$ m/s (same bubble than Fig. B.25), flowing from right to left.

B.2. Velocity and size measurement

In addition to the images described above, 640 × 320 pixels images were recorded in order to calculate the size and velocity of the elongated bubbles. With this resolution at 3200 FPS a maximum of 17 s can be recorded with the camera used for the measurements. This implies 54,400 frames per run. Again, background subtraction and histogram stretching is performed, and a line-scan image is constructed to identify nose and tail locations following the procedure described in Section 2.3.1. Then, for each bubble an interrogation window including the nose or tail of the bubble is extracted and cross-correlated with an image taken a few milliseconds later. In this way a displacement is calculated for the maximum correlation coefficient obtained. Fig. B.25 shows an example for a bubble for $j_g = 1.02$ and $j_f = 1$ m/s. In Figs. B.25a and B.25b the interrogation windows enclosing the nose and tail are indicated with dashed lines respectively. Figs. B.25c and B.25d correspond to tenth subsequent frames of Figs. B.25a and B.25d respectively, and the red rectangles indicate where the maximum correlation coefficient is found between the interrogation window and the current frame.

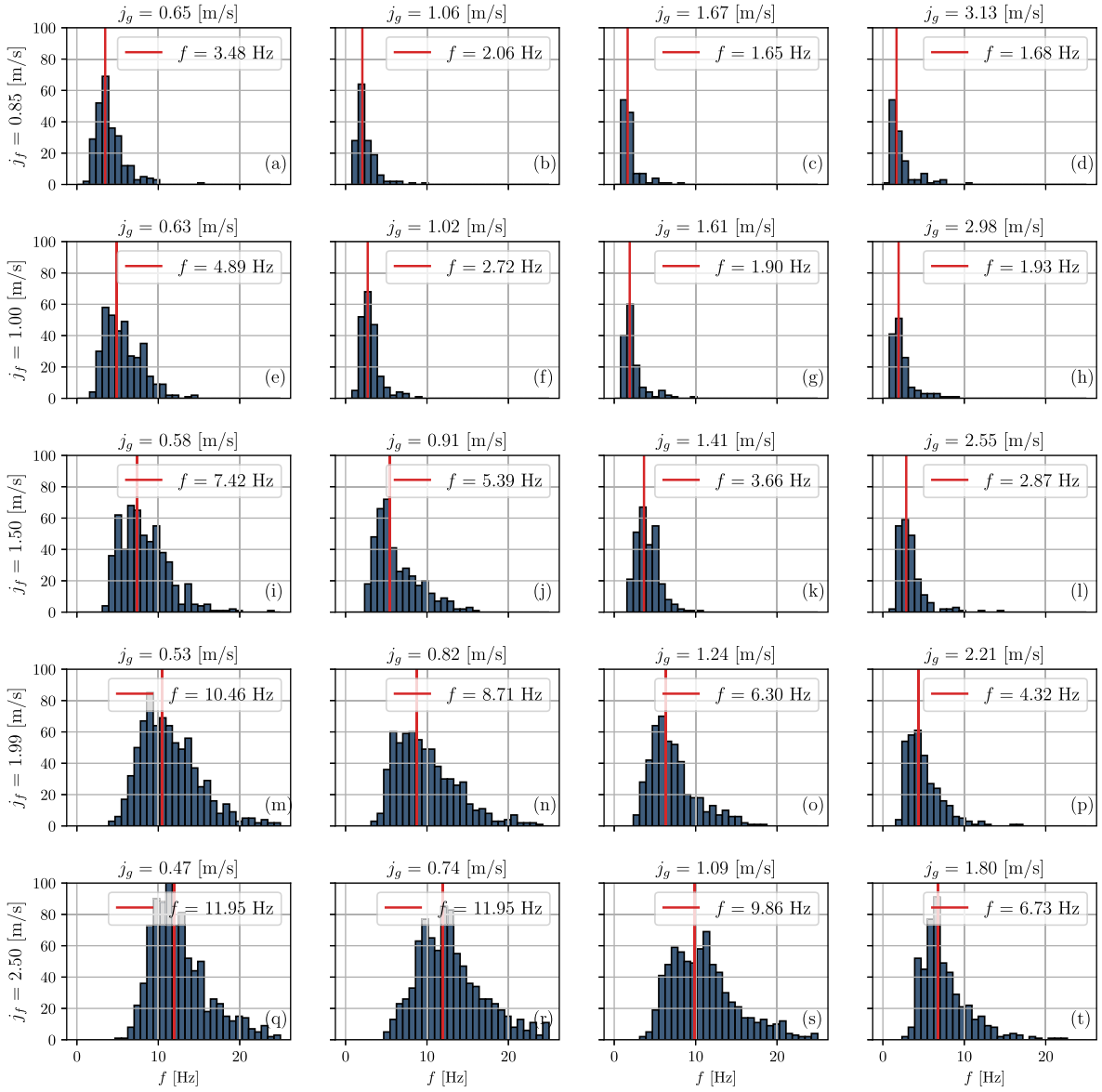

Fig. C.28. Histograms of measured slug frequencies for two-phase flow.

B.2.1. Sensitivity analysis

As digital images are made up of pixels, the distance between the black and red rectangles in Fig. B.25 is measured in whole units of pixels. Therefore, the measure of displacement of the nose or tail of the bubble is obtained in a discrete domain. The sensitivity analyses of the nose and tail velocities as a function of the jump (number of frames between the two images) are presented in Figs. B.26a and B.26b, respectively. The black dots indicate the velocity of the nose (or tail) calculated at the corresponding jump (x axis), and the blue dots indicate the correlation factor between the interrogation window and subsequent frames. As the jump increases the similarity between the original interrogation window and all subsequent frames decreases, so does the correlation factor (blue dots), as expected.

For lower values of frame jumps (between 1 and 6) the velocities show some oscillations. This is expected, because the interrogation window is displaced one pixel at a time while the captured bubble is moving in real domain, and so in subsequent frames the displacement can actually correspond to fractions of pixels. In both images of Fig. B.26, the velocity becomes stable at jumps of about 10 frames. However, for bigger jumps, of more than 20 frames, the bubbles may adopt shapes that are different than the one in the interrogation window and higher oscillations can be found, especially at the tail, where several bubbles get detached from the tail of the bubble and the shape may then vary significantly. Using a jump value of 10 frames, correlation factors of 0.85 and 0.66 are obtained for the nose and tail, respectively. The correlation factor for the tail images drops much faster than in the nose images. This is due to the presence of several drops detaching from the tail, which changes the shapes in the image more rapidly.

B.2.2. Validation

Furthermore, the images for the velocity analysis were taken with a ruler attached to the pipe. This allows to calibrate the pixel size, and to manually compare the velocity calculations using the automated algorithm. Fig. B.27 shows two images taken with the ruler attached to the pipe as a reference.

In Fig. B.27a the axial position of the nose of an elongated bubble is marked with a red dashed line at 11.5 cm in the ruler. In Fig. B.27b the

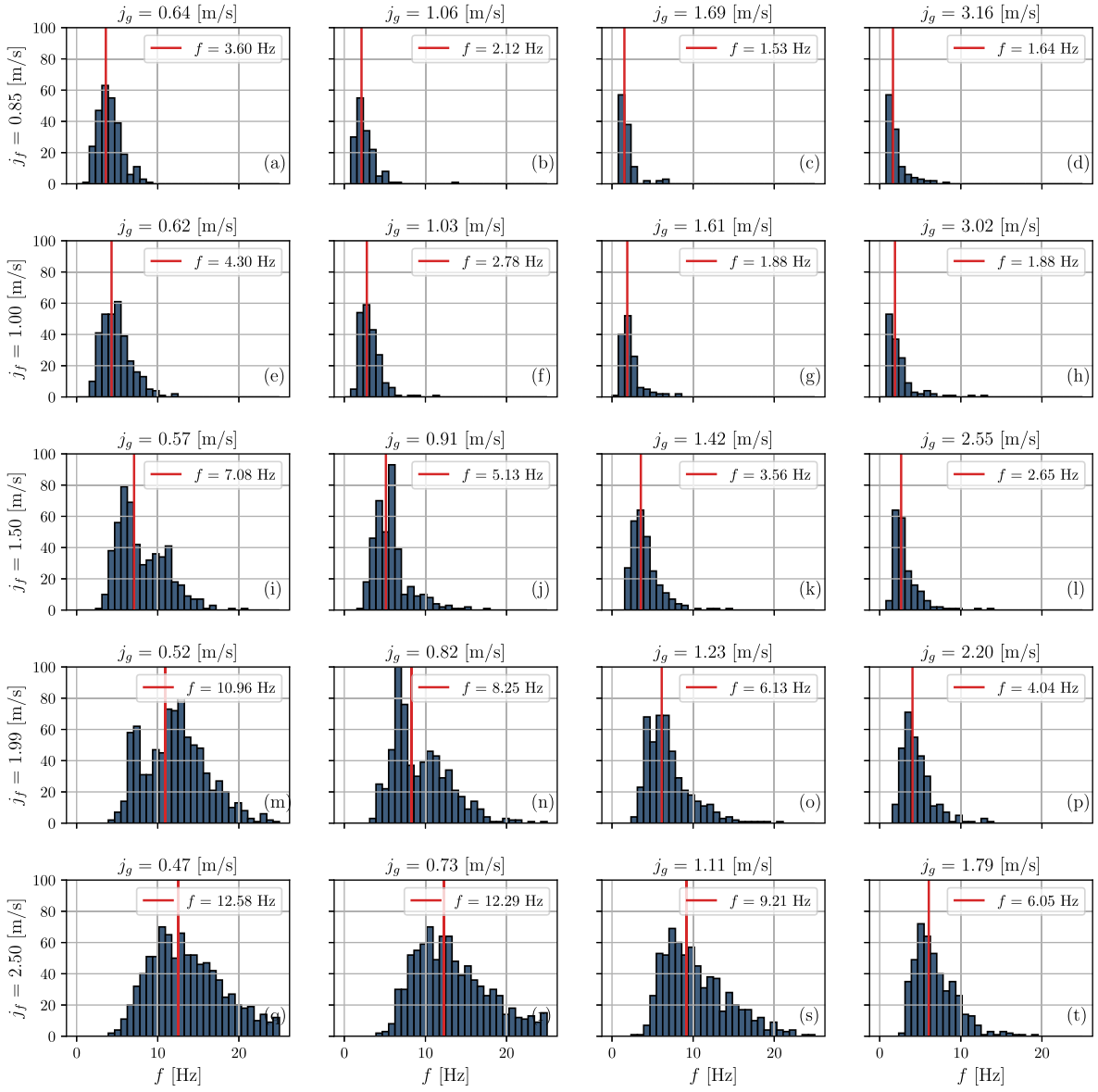

Fig. C.29. Histograms of measured slug frequencies for three-phase flows with 10% of solid concentration.

same bubble is marked 133 frames later at 21 cm in the ruler. In this way it is possible to calculate the velocity of the nose with Eqs. (B.1) and (B.2) where Δx represents the distance between the red lines in meters, measured with the ruler. The velocity obtained applying the algorithm for the corresponding nose is 2.26 m/s, with a relative error of about 6%.

$$\Delta t = \frac{N_{frames}}{FPS} = \frac{126}{3200} \tag{B.1}$$

$$V_{nose} = \frac{\Delta x}{\Delta t} = \frac{0.095}{0.0394} = 2.41 \text{ m/s} \tag{B.2}$$

This calculation has been done manually for several noses and tails chosen at random, and the average relative error is about 5%.

In order to establish the pixel size, the quotient between the amount of pixels between the red lines (551) and the corresponding distance (0.095 m) is calculated, obtaining a pixel size of 0.1724 mm/px. This is calculated for every setting of the camera, whose position may vary a few millimeters between measurements.

B.2.3. Bubble length

Finally, the length of the bubbles is determined with Eq. (B.3), using the mean velocity of each bubble ($\bar{U_b}$) and the residence time of the corresponding bubble in the cross section ($t_1 - t_0$) of the line-scan image. Where t_0 is the instant of time in which the nose intersects the cross section, and t_1 when the tail intersects it. ($t_1 - t_0$) corresponds to the distance in pixels between a blue line and the consecutive red line in the line-scan image (Fig. 4) divided by the frame rate.

$$L_b = \bar{U_b} \cdot (t_1 - t_0) \tag{B.3}$$

Appendix C. Distribution of frequencies

In Figs. C.28 to C.30 the histograms of the inverse of the permanence time (frequency) of the slug units are illustrated for all the two and three-phase runs with 10% and 20% of solid loading, respectively.

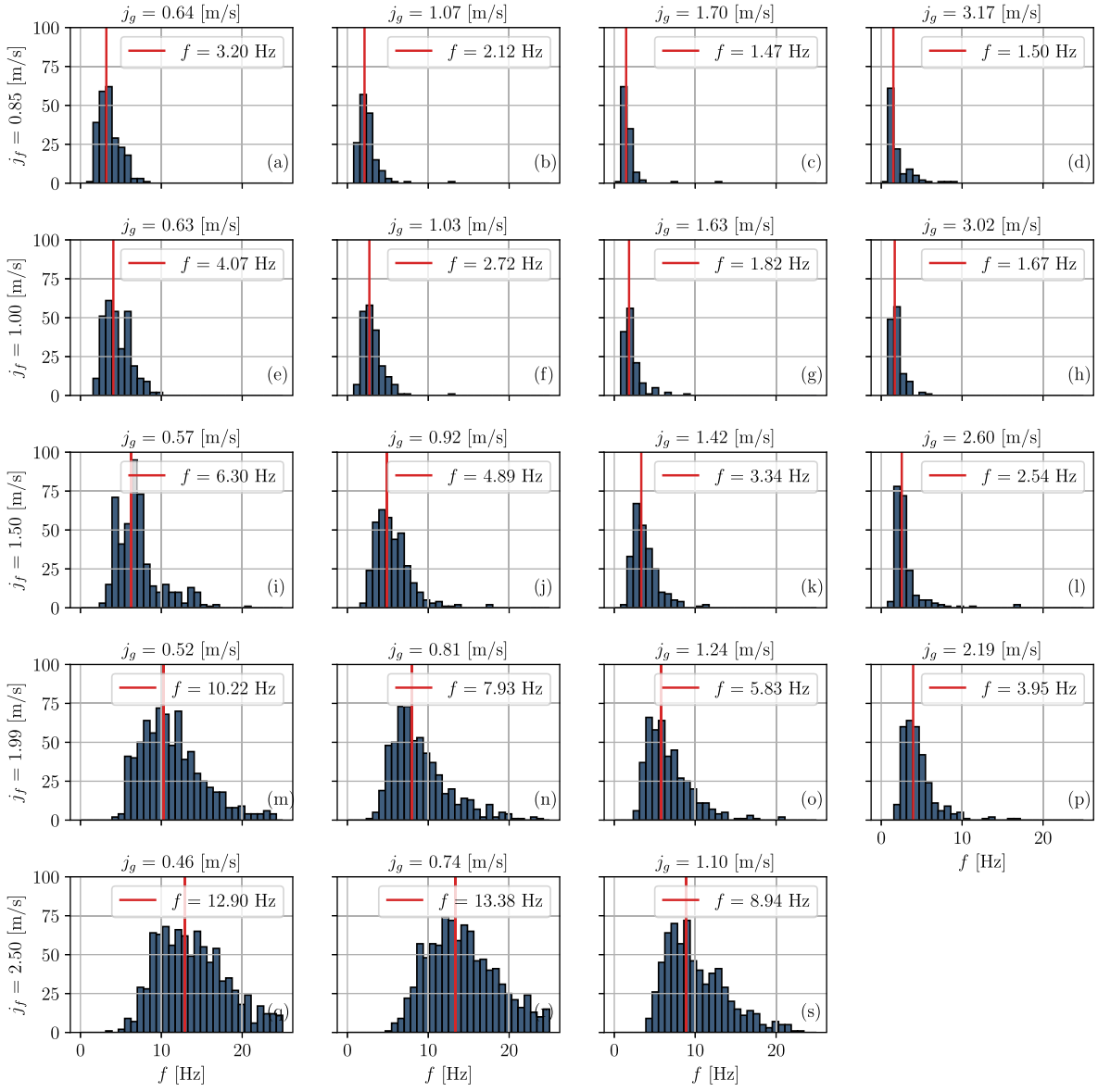

Fig. C.30. Histograms of measured slug frequencies for three-phase flows with 20% of solid concentration.

References

Akhlaghi, M., Mohammadi, V., Nouri, N.M., Taherkhani, M., Karimi, M., 2019. Multi-Fluid VoF model assessment to simulate the horizontal air–water intermittent flow. Chem. Eng. Res. Des. 152, 48–59. http://dx.doi.org/10.1016/j.cherd.2019.09.031.

Al-Alweet, F.M., Jaworski, A.J., Alghamdi, Y.A., Almutairi, Z., Kołłątaj, J., 2020. Systematic frequency and statistical analysis approach to identify different gas-liquid flow patterns using two electrodes capacitance sensor: Experimental evaluations. Energies 13 (11), http://dx.doi.org/10.3390/en13112932.

Al-Kayiem, H.H., Mohmmed, A.O., Al-Hashimy, Z.I., Time, R.W., 2017. Statistical assessment of experimental observation on the slug body length and slug translational velocity in a horizontal pipe. Int. J. Heat Mass Transfer 105, 252–260. http://dx.doi.org/10.1016/j.ijheatmasstransfer.2016.09.105.

Al-Safran, E., 2009. Investigation and prediction of slug frequency in gas/liquid horizontal pipe flow. J. Pet. Sci. Eng. 69 (1–2), 143–155. http://dx.doi.org/10.1016/j.petrol.2009.08.009.

Al-Safran, E.M., 2016. Probabilistic modeling of slug frequency in gas/liquid pipe flow using the Poisson probability theory. J. Pet. Sci. Eng. 138, 88–96. http://dx.doi.org/10.1016/j.petrol.2015.12.008.

Arabi, A., Azzi, A., Kadi, R., Al-Sarkhi, A., Hewakandamby, B., 2021. Empirical modelization of intermittent gas/liquid flow hydrodynamic parameters: The importance of distinguishing between plug and slug flows. SPE Prod. Oper. 36 (03), 703–720. http://dx.doi.org/10.2118/205481-PA, arXiv:https://onepetro.org/PO/article-pdf/36/03/703/2475062/spe-205481-pa.pdf.

Arabi, A., Ragui, K., Salhi, Y., Filali, A., 2020a. Slug frequency for a gas-liquid plug flow: Review and development of a new correlation. Int. Commun. Heat Mass Transfer 118, 104841. http://dx.doi.org/10.1016/j.icheatmasstransfer.2020.104841.

Arabi, A., Salhi, Y., Zenati, Y., Si-Ahmed, E.K., Legrand, J., 2020b. On gas-liquid intermittent flow in a horizontal pipe: Influence of sub-regime on slug frequency. Chem. Eng. Sci. 211, 115251. http://dx.doi.org/10.1016/j.ces.2019.115251.

Archibong-Eso, A., Baba, Y., Aliyu, A., Zhao, Y., Yan, W., Yeung, H., 2018. On slug frequency in concurrent high viscosity liquid and gas flow. J. Pet. Sci. Eng. 163 (September 2017), 600–610. http://dx.doi.org/10.1016/j.petrol.2017.12.071.

Bertola, V., Cafaro, E., 2002. Slug frequency measurement techniques in horizontal gas-liquid flow. AIAA J. 40 (5), 1010–1012. http://dx.doi.org/10.2514/2.1742.

Bhagwat, S.M., Ghajar, A.J., 2014. A flow pattern independent drift flux model based void fraction correlation for a wide range of gas-liquid two phase flow. Int. J. Multiph. Flow. 59, 186–205. http://dx.doi.org/10.1016/j.ijmultiphaseflow.2013.11.001.

Dabirian, R., Mohammadikharkeshi, M., Mohan, R., Shoham, O., 2019. Critical sand deposition velocity in intermittent flow - models evaluation. In: Proceedings - SPE Annual Technical Conference and Exhibition, Vol. 2019-Septe. http://dx.doi.org/10.2118/196085-ms.

Dabirian, R., Mohan, R.S., Shoham, O., 2017. CFD simulation of critical sand deposition velocity for solid-liquid slurry flow. In: Proceedings - SPE Annual Technical Conference and Exhibition. http://dx.doi.org/10.2118/187049-ms.

Dabirian, R., Padsalgikar, A., Mohan, R.S., Shoham, O., 2018. Four-layer model for prediction of sand bed height in horizontal gas-liquid stratified flow. J. Pet. Sci. Eng. 165, 151–160. http://dx.doi.org/10.1016/j.petrol.2018.02.022.

Danielson, T.J., 2007. Sand transport modeling in multiphase pipelines. http://dx.doi.org/10.4043/18691-ms.

Deendarlianto, Rahmandhika, A., Widyatama, A., Dinaryanto, O., Widyaparaga, A., Indarto, 2019. Experimental study on the hydrodynamic behavior of gas-liquid air-water two-phase flow near the transition to slug flow in horizontal pipes. Int. J. Heat Mass Transfer 130, 187–203. http://dx.doi.org/10.1016/j.ijheatmasstransfer.2018.10.085.

Fetter, C., 1988. Development of a Clamp-On Acoustic Two-Phase Flowmeter (Master thesis). Technical University Delft, URL: http://resolver.tudelft.nl/uuid:a3e8c0c1-4f45-4399-b327-f11fb18db149.

Fossa, M., Guglielmini, G., Marchitto, A., 2003. Intermittent flow parameters from void fraction analysis. Flow Meas. Instrum. 14 (4–5), 161–168. http://dx.doi.org/10.1016/S0955-5986(03)00021-9.

Godhavn, J.M., Fard, M.P., Fuchs, P.H., 2005. New slug control strategies, tuning rules and experimental results. J. Process Control 15 (5), 547–557. http://dx.doi.org/10.1016/j.jprocont.2004.10.003.

Gregory, G.A., Scott, D.S., 1969. Correlation of liquid slug velocity and frequency in horizontal cocurrent gas-liquid slug flow. AIChE J. 15 (6), 933–935. http://dx.doi.org/10.1002/aic.690150623, URL: https://aiche.onlinelibrary.wiley.com/doi/abs/10.1002/aic.690150623.

Hout, R.V., Barnea, D., Shemer, L., 2002. Translational velocities of elongated bubbles in.pdf. 28, 1333–1350.

Ibarra, R., Mohan, R.S., Shoham, O., 2017. Investigation of critical sand-deposition velocity in horizontal gas/liquid stratified flow. SPE Prod. Oper. 32 (3), 218–227. http://dx.doi.org/10.2118/168209-pa.

Kong, R., Kim, S., Bajorek, S., Tien, K., Hoxie, C., 2018a. Effects of pipe size on horizontal two-phase flow: Flow regimes, pressure drop, two-phase flow parameters, and drift-flux analysis. Exp. Therm Fluid Sci. 96 (December 2017), 75–89. http://dx.doi.org/10.1016/j.expthermflusci.2018.02.030.

Kong, R., Rau, A., Kim, S., Bajorek, S., Tien, K., Hoxie, C., 2018b. Experimental study of horizontal air-water plug-to-slug transition flow in different pipe sizes. Int. J. Heat Mass Transfer 123, 1005–1020. http://dx.doi.org/10.1016/j.ijheatmasstransfer.2018.03.027.

Kong, R., Zhu, Q., Kim, S., Ishii, M., Bajorek, S., Tien, K., Hoxie, C., 2018c. Void fraction prediction and one-dimensional drift-flux analysis for horizontal two-phase flow in different pipe sizes. Exp. Therm Fluid Sci. 99 (May), 433–445. http://dx.doi.org/10.1016/j.expthermflusci.2018.08.019.

Lin, M., Liu, Y., Hu, Y., Che, D., 2013. Influence of the gas and liquid superficial velocity on slug frequency. AIP Conf. Proc. 1547 (1), 253–263. http://dx.doi.org/10.1063/1.4816874.

Lockhart, R., Martinelli, R., 1949. Proposed correlation of data for isothermal two-phase, two-component flow in pipes. Chem. Eng. Prog. 45 (1), 39–48. http://dx.doi.org/10.1016/0017-9310(67)90047-6.

Lu, C., Kong, R., Qiao, S., Larimer, J., Kim, S., Bajorek, S., Tien, K., Hoxie, C., 2018. Frictional pressure drop analysis for horizontal and vertical air-water two-phase flows in different pipe sizes. Nucl. Eng. Des. 332 (September 2017), 147–161. http://dx.doi.org/10.1016/j.nucengdes.2018.03.036.

Manolis, I., Mendes-Tatsis, M., Hewitt, G., 1995. The Effect of Pressure on Slug Frequency in Two-Phase Horizontal Flow. Elsevier Science B.V., pp. 347–354. http://dx.doi.org/10.1016/b978-0-444-81811-9.50035-4.

Martínez, M., Vazquez, L., Vernet, A., Pallares, J., 2017. Numerical simulation of a three-phase flow with phase change in an industrial wall-heated flash line. In: 14th International Conference Multiphase Flow in Industrial Plant. Desenzano del Garda, Italy, pp. 1–8.

Pineda-Pérez, H., Kim, T., Pereyra, E., Ratkovich, N., 2018. CFD modeling of air and highly viscous liquid two-phase slug flow in horizontal pipes. Chem. Eng. Res. Des. 136, 638–653. http://dx.doi.org/10.1016/j.cherd.2018.06.023.

Rahman, M.A., Adane, K.F., Sanders, R.S., 2013. An improved method for applying the lockhart-martinelli correlation to three-phase gas-liquid-solid horizontal pipeline flows. Can. J. Chem. Eng. 91 (8), 1372–1382. http://dx.doi.org/10.1002/cjce.21843.

Rosas, L.M., Bassani, C.L., Alves, R.F., Schneider, F.A., Marcelino Neto, M.A., Morales, R.E., Sum, A.K., 2018. Measurements of horizontal three-phase solid-liquid-gas slug flow: Influence of hydrate-like particles on hydrodynamics. AIChE J. 64 (7), 2864–2880. http://dx.doi.org/10.1002/aic.16148.

Sassi, P., Pallarès, J., Stiriba, Y., 2020a. Visualization and measurement of two-phase flows in horizontal pipelines. Exp. Comput. Multiph. Flow 2 (1), 41–51. http://dx.doi.org/10.1007/s42757-019-0022-1, URL: https://link.springer.com/article/10.1007/s42757-019-0022-1#citeas.

Sassi, P., Stiriba, Y., Lobera, J., Palero, V., Pallarès, J., 2020b. Experimental analysis of gas–liquid–solid three-phase flows in horizontal pipelines. Flow Turbul. Combust. (0123456789), http://dx.doi.org/10.1007/s10494-020-00141-1.

Taitel, Y., Dukler, A., 1976. A theoretical approach to the lockhart-martinelli correlation for stratified flow. Int. J. Multiph. Flow. 2 (5–6), 591–595. http://dx.doi.org/10.1016/0301-9322(76)90019-7, URL: https://www.sciencedirect.com/science/article/pii/0301932276900197.

Talley, J.D., Worosz, T., Kim, S., Buchanan, J.R., 2015. Characterization of horizontal air – water two-phase flow in a round pipe part I : Flow visualization. Int. J. Multiph. Flow. 76, 212–222. http://dx.doi.org/10.1016/j.ijmultiphaseflow.2015.06.011.

Thaker, J., Banerjee, J., 2015. Characterization of two-phase slug flow sub-regimes using flow visualization. J. Pet. Sci. Eng. 135, 561–576. http://dx.doi.org/10.1016/j.petrol.2015.10.018.

Thaker, J., Banerjee, J., 2016a. Influence of intermittent flow sub-patterns on erosion-corrosion in horizontal pipe. J. Pet. Sci. Eng. 145, 298–320. http://dx.doi.org/10.1016/j.petrol.2016.05.006.

Thaker, J., Banerjee, J., 2016b. On intermittent flow characteristics of gas–liquid two-phase flow. Nucl. Eng. Des. 310, 363–377. http://dx.doi.org/10.1016/j.nucengdes.2016.10.020.

Thaker, J., Banerjee, J., 2017. Transition of plug to slug flow and associated fluid dynamics. Int. J. Multiph. Flow. 91, 63–75. http://dx.doi.org/10.1016/j.ijmultiphaseflow.2017.01.014.

Wang, X., Guo, L., Zhang, X., 2007. An experimental study of the statistical parameters of gas-liquid two-phase slug flow in horizontal pipeline. Int. J. Heat Mass Transfer 50 (11–12), 2439–2443. http://dx.doi.org/10.1016/j.ijheatmasstransfer.2006.12.011.

Wilkens, R.J., Thomas, D.K., 2008. A simple technique for determining slug frequency using differential pressure. J. Energy Resour. Technol. 130 (1), http://dx.doi.org/10.1115/1.2824297.

Xu, K.W., Zhang, Y., Liu, D., Azman, A.N., Kim, H.B., 2020. Slug flow development study in a horizontal pipe using particle image velocimetry. Int. J. Heat Mass Transfer 162, 120267. http://dx.doi.org/10.1016/j.ijheatmasstransfer.2020.120267.

Zhai, S., Pang, S., Shao, J., Zhu, H., Zhang, X., Liu, P., 2018. The FAC experimental research on vapor-water two-phase flow piping system of CAP1400 secondary loop. MATEC Web Conf. 207, 1–8. http://dx.doi.org/10.1051/matecconf/201820704001.